Available online at www.sciencedirect.com
ScienceDirect
Journal of Nuclear Materials 375 (2008) 290–310
journal of nuclear materials
www.elsevier.com/locate/jnucmat

Corrosion of UO_2 and ThO_2: A quantum-mechanical investigation

F.N. Skomurski [a,*], L.C. Shuller [b], R.C. Ewing [a,b], U. Becker [a]

[a] Department of Geological Sciences, University of Michigan, 2534 C.C. Little Building, 1100 N. University Avenue, Ann Arbor, MI 48109, USA
[b] Department of Materials Science and Engineering, University of Michigan, H.H. Dow, 2300 Hayward Street, Ann Arbor, MI 48109, USA

Received 11 June 2007; accepted 20 December 2007

Abstract

The addition of Th to U-based fuels increases resistance to corrosion due to differences in redox-chemistry and electronic properties between UO_2 and ThO_2. Quantum-mechanical techniques were used to calculate surface energy trends for ThO_2, resulting in (1 1 1) < (1 1 0) < (1 0 0). Adsorption energy trends were calculated for water and oxygen on the stable (1 1 1) surface of UO_2 and ThO_2, and the effect of model set-up on these trends was evaluated. Molecular water is more stable than dissociated water on both binary oxides. Oxidation rates for atomic oxygen interacting with defect-free UO_2(1 1 1) were calculated to be extremely slow if no water is present, but nearly instantaneous if water is present. The semi-conducting nature of UO_2 is found to enhance the adsorption of oxygen in the presence of water through changes in near-surface electronic structure; the same effect is not observed on the insulating surface of ThO_2.

PACS: 28.41.Kw; 28.41.Vx; 31.15.Ar; 31.15.Ew; 68.43.−h; 68.43.Bc; 68.43.Fg; 63.43.Mn; 82.65.+r

1. Introduction

UO_2 and ThO_2 are the end-members of a binary system that forms a complete solid solution with the isometric fluorite structure [1]. As a result, ThO_2 can be used as fertile nuclear fuel material in light water reactors when mixed with a fissile component such as ^{235}U [2]. Although both binary oxides have the cubic fluorite structure ($\mathbf{a} = 0.5468$ nm for UO_2; $\mathbf{a} = 0.5597$ nm for ThO_2 [3]), U and Th have very different electronic and chemical properties that ultimately affect the interaction of UO_2 and ThO_2 with adsorbates, such as water and oxygen. For instance, U has four oxidation states (3+ through 6+), and in UO_2, each U^{4+} has two unpaired 5f valence electrons which give rise to the band gap of approximately 2 eV [4]. The oxidation of UO_2 to form UO_{2+x} contributes to the weak, p-type semi-conducting nature of UO_2 [5]. In contrast, Th only has one oxidation state (4+) and due to the absence of 5f electrons in the valence band, ThO_2 is an insulator with a band gap of 6 eV [5]. The multiple oxidation states of U and the ability of UO_2 to incorporate interstitial oxygen into the cubic fluorite structure make it more susceptible to corrosion than ThO_2, where excess oxygen cannot be added to the structure without the creation of defects or the addition of impurities [2,6]. However, studies demonstrate that with the addition of enough Th to the UO_2, resistance to oxidation increases while dissolution rates decrease [7–9]. Such properties are attractive for spent nuclear fuel as a waste-form in a once-thought fuel cycle.

Numerous spectroscopic studies have been completed in order to investigate the behavior of water and oxygen with UO_2 and pure uranium metal surfaces [10–21]. Pure UO_2 and U-based spent nuclear fuel (SNF) have a strong tendency to oxidize in the presence of oxygen and radiolytic oxidants such as H_2O_2, $OH^{\cdot}$, and HO_2 [22–26]. Surface-specific studies show that the occurrence of molecular *versus* dissociated water on UO_2(1 1 1) and (1 0 0) surfaces varies as a function of surface structure, defect concentration,

* Corresponding author. Present address: Chemical and Materials Sciences Division, Pacific Northwest National Laboratory, P.O. Box 999, MS K8-96, 3335 Q St., Richland, Washington 99352, USA. Tel.: +1 509 371 6368; fax: +1 509 376 3650.
E-mail address: frances.skomurski@pnl.gov (F.N. Skomurski).

0022-3115/$ - see front matter © 2008 Elsevier B.V. All rights reserved.
doi:10.1016/j.jnucmat.2007.12.007

and the use of polycrystalline *versus* single-crystal substrates [16,19–21,27]. The presence of defects or the use of polycrystalline materials tends to favor the dissociation of water [19] which is important because the interaction of water with actinide–oxide surfaces (e.g. PuO_2) can potentially produce free H_2 gas under anoxic conditions *via* the dissociation of water [28]. Furthermore, once a fuel rod is breached, water can accelerate the corrosion process in an oxidizing environment [22,26] leading to the formation of higher oxide phases accompanied by volume changes, fuel cladding failure, and ultimately radionuclide release [24].

Experimental investigations have also been performed on ThO_2 and metallic Th [6,12,29–33]. Although ThO_2 is resistant to oxidation, ThO_2 surfaces still interact strongly with water and have a tendency to become hydroxylated [6,30,31]. Although ThO_2 is a viable nuclear fuel material, modern experimental techniques (e.g. thermal desorption spectroscopy) have not been applied to the investigation of adsorbate evolution on specific ThO_2 surfaces in the same detail as for UO_2.

Recently, atomic-scale quantum-mechanical and empirical-potential calculations have been used to determine relative surface reactivity [34,35] and stable surface terminations [36] of a variety of UO_2 and PuO_2 surfaces. Similar calculations have been used to simulate the hydroxylation of UO_2 surfaces and to calculate the resulting adsorption energies as a function of surface termination [37–39]. Hydroxylation of actinide–oxide surfaces (ThO_2, UO_2 and PuO_2) has been explored as a function of electronic structure [40]. By using computational techniques to understand the very first interactions between actinide–oxide surfaces and environmental molecules, the stability of these materials can be better assessed over the range of environmental conditions expected in storage and disposal environments, such as variations in redox potential, pH, and humidity.

In order to better understand the differences in corrosion resistance between UO_2 and ThO_2, in this study surface–adsorbate interactions are explored as a function of substrate chemistry and electronic structure using quantum-mechanical techniques. First, the relative stabilities of the low-index (1 1 1), (1 1 0), and (1 0 0) surfaces of UO_2 and ThO_2 were determined using quantum-mechanical surface-energy calculations. Adsorption energies were then calculated for four adsorption cases on the stable (1 1 1) surface of each material: (1) one-half mono-layer (ML) of molecular water, (2) one-half ML of dissociated water, (3) one-half ML of dissociated O_2, and (4) a combined molecular water and dissociated O_2 case that is meant to simulate more realistic corrosion conditions. The effect of adsorbate coverage on adsorption energy trends was tested by comparing adsorption energies for full-ML of water and dissociated water on a UO_2 slab. Those full-ML models were also used to determine the effect of model set-up on adsorption energy values (e.g. energy contributions due to dipole-moment formation when using single, rather than double-sided adsorption models).

Although UO_2 is not a semi-conductor in the same sense as Si or Ge, electron mobility in this material plays a significant role in the mechanisms and energetics of redox processes. Studies indicate that the near-surface region of even weakly semiconducting materials can serve as a catalytic conductor between oxidant and reductant [41–43]. The focus of this investigation is to provide a quantum-mechanical understanding of corrosion processes for specific actinide–oxide surfaces and to explain corrosion behavior as a function of the electronic and spin structure of the metal in the oxide. These results provide a basis for interpreting experimental results related to the enhancement of the corrosion of UO_2 surfaces within the stability field of water (molecular or dissociated) [17].

2. Methods

2.1. Calculation parameters

The density functional theory-based (DFT) [44,45] quantum-mechanical code, CASTEP (CAmbridge Serial Total Energy Package), was used to perform all surface energy and adsorption energy calculations. In DFT, the ground-state total energy of the system is related to its ground-state electron density [46], and in CASTEP, planewaves are used as basis sets to model the wavefunctions that describe the distribution of electrons in the system. To capture the distribution of valence-electron density between different atoms, the spin-polarized generalized gradient approximation (GGA-PW91) [47] was used rather than the spin-polarized local density approximation, based on better agreement of optimized lattice parameters with experimental data (see Table 1). Ultra-soft pseudopotentials that account for relativistic corrections, which are important for the actinide elements, were used such that only electrons from U 5f,6s, 6p, 6d, 7s, Th 6s, 6p, 6d, 7s, O 2s, 2p, and H 1s orbitals had to be explicitly treated. Surface-energy calculations for ThO_2 were performed using a version of CASTEP that is part of the modeling package, Cerius^2 (CASTEP Version 4.6, 2001) [48] for comparison with published surface energy results for UO_2 in [35]. All electronic structure and adsorption energy calculations were performed using a more recent version of CASTEP (Version 4.0) [49], which is part of the Materials Studio Modeling package 4.0. Parameter space testing of optimal *k*-point spacing, planewave energy cut-off, and different density functionals (e.g. GGA-PW91 *versus* LDA) was performed on conventional cubic unit cells of UO_2 and ThO_2, each containing four formula units.

2.2. Surface energy calculations

Surface energy calculations for the ThO_2 (1 1 1), (1 1 0), and (1 0 0) surfaces were performed in the same fashion as those for UO_2 in a previous publication [35]. A conventional unit cell of ThO_2 was optimized using space group symmetry ($Fm\bar{3}m$), an energy cut-off of 460 eV, and a

Table 1
Results from parameter space testing involving conventional UO_2 and ThO_2 unit cells

Compound	Spin functional	Plane-wave cut-off (eV)	Number of *k*-points	Optimized lattice parameters (nm)	Total energy (eV)
UO_2	PW91-GGS	550	1	0.5468	−9178.96
UO_2	PW91-GGS	550	4	0.5455	−9178.95
UO_2	PW91-GGS	750	1	0.5466	−9179.39
UO_2	PW91-GGS	750	4	0.5466	−9179.36
ThO_2	PW91-GGA	550	1	0.5584	−7506.09
ThO_2	PW91-GGA	550	4	0.5584	−7506.04
ThO_2	PW91-GGA	750	1	0.5590	−7505.95
ThO_2	PW91-GGA	750	4	0.5590	−7505.91

Note: PW91-GGS and -GGA refer to spin-functionalized and spin-free versions of the Perdew and Wang generalized gradient approximation [47].

k-point spacing of 0.01 nm^{-1}. This spacing corresponds to one *k*-point at (0.25, 0.25, 0.25) within the irreducible Brillouin zone. Surface slabs of increasing thickness were 'cleaved' from the optimized bulk, parallel to the three crystallographic directions of interest. For a schematic view and in-depth description of each surface structure, see [35]. The use of planewaves in the CASTEP code necessitates the use of three-dimensional periodic boundary conditions; hence, a 1.0 nm vacuum gap between the surface slabs is used to simulate a free surface while maintaining an infinitely periodic structure [50]. The same energy cut-off and *k*-point spacing that were used for bulk optimization were used for the slabs, however *P*1 symmetry was imposed on the slabs so that there would not be symmetry constraints on atomic movement during relaxation and adsorption. The use of *P*1 symmetry results in 5 *k*-points within the irreducible Brillouin zone for the (1 1 1) and (1 0 0) slabs, and 3 *k*-points for the (1 1 0) slab. During geometric optimization, lattice parameters parallel to the slab surface (***a*** and ***b***) were held constant to simulate the constraining force of an underlying bulk structure, and the vacuum gap in the *z*-direction was maintained by holding ***c*** constant. Surface energies were calculated from optimized slab energies according to the theory described in previous publications [35,51]. Surface energy is the excess energy per unit area as compared to the bulk structure due to the presence of dangling bonds and the lower coordination of atoms at the surface.

2.3. Adsorption energy calculations

Surface slab models were generated by cleaving perpendicular to the ⟨1 1 1⟩ direction in bulk UO_2 and ThO_2 ($\boldsymbol{a} = 0.5468$ nm and $\boldsymbol{a} = 0.5597$ nm, respectively). This surface is a Tasker II-type surface, composed of stoichiometric 'sandwich' layers of oxygen–metal–oxygen packages that are stacked on top of one another [52,53], and the natural cleavage plane of fluorite-type materials occurs between the two consecutive anion layers. Each slab had a thickness of two stoichiometric units, corresponding to 0.4735 nm for UO_2 and 0.4847 nm for ThO_2. A vacuum gap of 1.5 nm was placed perpendicular to the slab surface (along the *z*-direction) in order to simulate a free surface in a periodic environment (see Fig. 1). This vacuum gap allowed for a distance of at least 1.0 nm to be maintained between slabs when adsorbates were added. Increasing the vacuum gap from 1.5 to 2.0 nm did not lead to any significant changes in slab energies for UO_2 (0.006 eV lower) or ThO_2 (0.001 eV lower). A double-sided adsorption approach was used in order to avoid the formation of a dipole moment perpendicular to the slab surface [54]. Such a dipole moment would lead to interaction energies between slabs, creating an artifact addition to the adsorption energy (see Appendix A).

Both half and full-ML adsorption models were used in this study, but only half-ML models are shown in Fig. 1. On the (1 1 1) surface, one adsorption site above a metal cation exists per $\sim 0.4\ \text{nm} \times 0.4\ \text{nm} \times \sin 120°$ area of the slab. To create models with half-ML coverage, slabs were doubled in the *x*-direction ($\sim 0.8\ \text{nm} \times 0.4\ \text{nm} \times \sin 120°$) to generate two adsorption sites per surface. For full-ML cases, all of the surface-sites of a single slab were occupied, corresponding to 0.21 mg of H_2O per m^2, and for the half-ML cases, half the sites of a doubled slab were occupied for an adsorption density of 0.11 mg of H_2O per m^2. For cases involving the adsorption of molecular water, one molecule was placed above a near-surface U or Th atom in an upright position at a distance of 0.25 nm (Fig. 1a). For dissociated water, an OH^- group (spin = 0) was placed above a near-surface cation at a distance of 0.22 nm, and the dissociated H^+ atom (spin = 0) was placed on a neighboring surface O atom at a distance of 0.098 nm (Fig. 1b). Oxygen adsorption models assume that O_2 has dissociated and atomic O is placed above a near-surface cation at a distance of ~0.2 nm (Fig. 1c). Different spin configurations are discussed in Section 3. In the co-adsorption case, atomic oxygen and molecular water are placed on the same side of the slab, at the distances listed above (Fig. 1d).

In order to calculate adsorption energies for each case, total energy values from three separate models were needed: (1) the adsorbate-free slab, (2) the adsorbate-covered slab, and (3) the adsorbing molecule by itself (e.g. H_2O and O_2). For these calculations, an energy cut-off of 550 eV and a *k*-point spacing of 0.007 nm^{-1} were used, corresponding to 4 symmetrically unique *k*-points for both bulk and surface slab calculations when *P*1 symmetry is applied. These parameters were chosen so that changes in bulk energy and optimized lattice parameters were

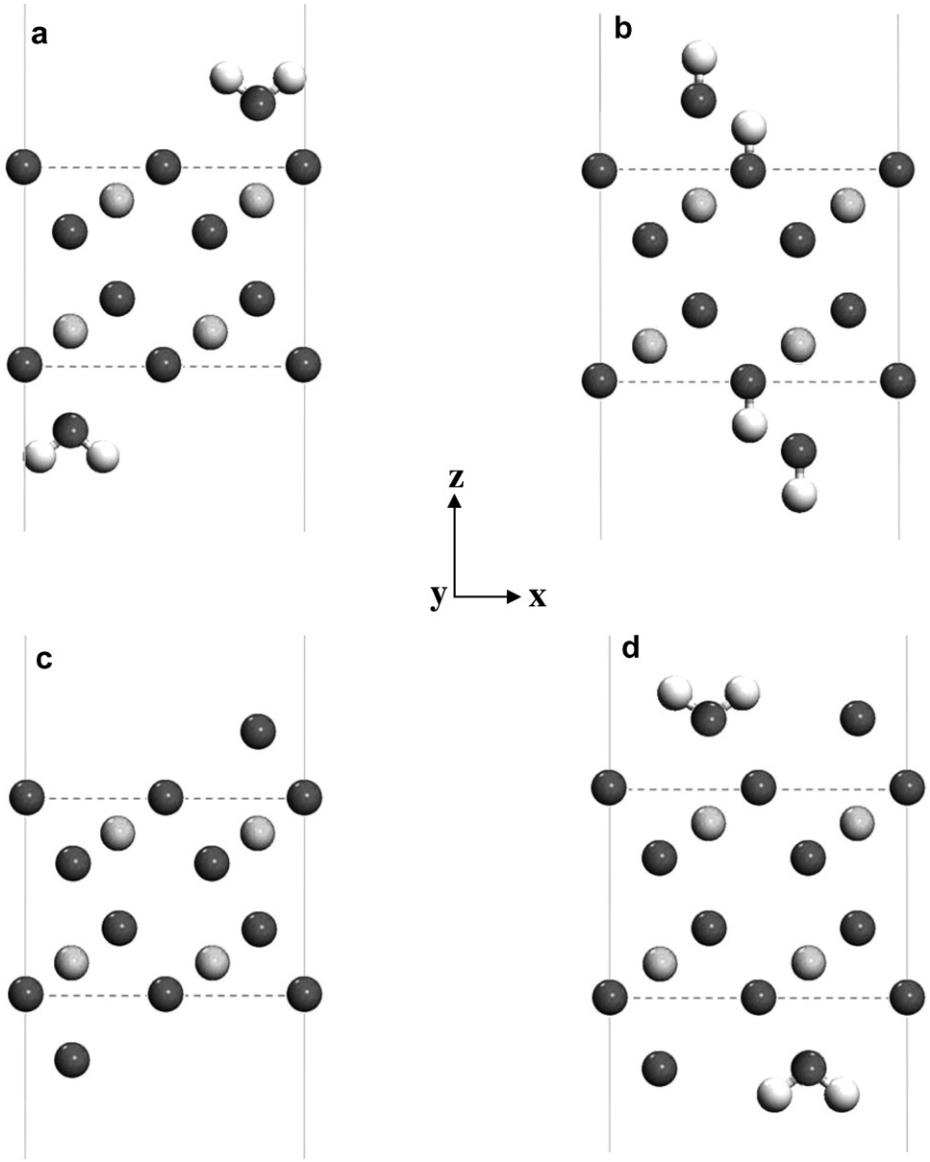

Fig. 1. Models depicting starting orientations of adsorbates on the (1 1 1) surface of UO_2 and ThO_2, with half-ML coverage of (a) molecular water, (b) dissociated water, (c) atomic O, and (d) full-ML of molecular water and atomic O. Gray spheres represent U or Th, dark spheres represent O, and white spheres represent H. All slabs are two stoichiometric units thick. The dotted line at the top and bottom of the slab is parallel to the (1 1 1) surface, and the 1.5 nm vacuum gap is perpendicular to this surface in the *z*-direction.

minimized upon further increases in the cut-off energy and *k*-point density (see Table 1). During optimization of the slab models (with and without adsorbates), lattice parameters were held constant in the ***a***, ***b***, and ***c***-directions while all atoms were allowed to relax. An inversion center (symmetry *P*-1) was applied to charge transfer cases involving oxygen on the UO_2 surface in order to better maintain slab geometry upon oxidation. The number of empty bands used in density-of-states (DOS) calculations was 12 for ThO_2 and 24 for UO_2, as more empty bands are needed to account for the partial filling of energy levels above the Fermi level (E_F) in UO_2 than in ThO_2.

The total energy of each adsorbate in its molecular form (e.g. H_2O and O_2) was calculated by placing each molecule in a $1 \times 1 \times 1\ nm^3$ box. This box size is large enough to eliminate consideration of molecule–molecule interactions in an infinitely periodic set-up. Each molecule was allowed to relax using the same planewave energy cut-off and *k*-point spacing as was used in the adsorption energy calculations. For molecular oxygen, the triplet state was found to be more energetically favorable than the singlet state in accordance with O_2 being paramagnetic. For cases involving the adsorption of atomic oxygen, high-spin and low-spin models were tested for both UO_2 and ThO_2, and an additional charge transfer model was tested for UO_2. Information regarding spin distribution is provided in Section 3 of this paper where oxygen adsorption cases are discussed. Unless otherwise noted, all uranium atoms were treated as U^{4+} and are assigned a spin of 2 to represent the two unpaired electrons in the 5f orbitals. Spin numbers in this

paper are referred to as the number of unpaired spins; each unpaired spin carries an orbital momentum of $\hbar/2$, where $\hbar = h/2\pi$ and h is Planck's constant. Spin and charge values were optimized from their starting values during the quantum-mechanical runs by providing a sufficient number of empty states and running the calculation in metal mode (the resulting structure can still have a finite band gap and, thus, be an insulator or metal).

The following equation was used to calculate the adsorption energy for each case:

$$E_{ads} = \frac{1}{2}(E_{slab+adsorbate} - E_{slab} - E_{adsorbate}). \quad (1)$$

Here, $E_{slab+adsorbate}$ represents the total calculated energy of the slab plus adsorbates, E_{slab} is the energy of the optimized slab without adsorbates, and $E_{adsorbate}$ is the internal energy of each adsorbate (e.g. molecular water or molecular oxygen). Molecular H_2O and O_2 were the assumed starting phases, and final adsorption energies account for the dissociation of each molecule. The factor of '1/2' is used to calculate the adsorption energy for just one adsorbate, due to the use of a double-sided adsorption model. In this study, negative adsorption energies indicate that adsorption is favorable.

3. Results and discussion

3.1. Bulk structures and electronic properties

In order to compare the interaction of adsorbates with UO_2 and ThO_2 surfaces, it is instructive to first compare the electronic structures of the bulk materials. Results from geometric optimizations of the conventional unit cells of UO_2 and ThO_2 are shown in Table 1, and lattice parameters are within 0.25% of experimental values. These optimized unit cells were used to calculate the partial density of states (PDOS) for UO_2 and ThO_2. PDOS is the total density of states divided up into contributions from the s, p, d, and f orbitals, or the projections of the total DOS onto individual atomic orbitals (Fig. 2). As shown in Figs. 2(a) and (b), the main difference between the electronic structure of UO_2 and ThO_2 is the presence of unpaired U 5f electrons near the top of the valence band of UO_2 and the absence of Th 5f electrons in the same region for ThO_2. In its 4+ oxidation state, U loses two 7s, one 6d, and one 5f valence electrons, leaving two unpaired, highly localized 5f electrons in its valence shell, which are free to interact with adsorbates. In contrast, Th^{4+} assumes the stable radon configuration, losing two 6d and two 7s valence electrons [5], and the completely filled O 2p orbitals compose the top of the valence band. Due to the multiple oxidation states of U and the presence of unpaired electrons near the top of the valence band, UO_2 is more likely to react with oxidants than ThO_2.

Comparison with spectroscopy results indicates that the main bonding interactions between ⟨U–O⟩ and ⟨Th–O⟩ are captured by our PDOS results. Valence band photoemission (PES) and X-ray photoelectron spectroscopy (XPS) studies show that the main bonding interaction between the 6d and 7s orbitals of the actinides, and the 2p states of the oxygen, occurs at energies approximately 6 eV below the Fermi level [5,55]. In Fig. 2(a) and (b), an overlap of O 2p and actinide 6d and 7s energy states occurs approximately −1 to −5 eV below the Fermi level (0 eV) for ThO_2, and between −3 and −7 eV below the Fermi level for UO_2. Based on the pseudopotentials used, the Th 6s and U 6s are the lowest energy valence electron states to be calculated. The calculated energy eigenvalues of these states are approximately −39 eV below the Fermi level for ThO_2 and −43 to −45 eV below the Fermi level for UO_2. These values are close to experimentally observed values of −43 eV for ThO_2, and less than −45 eV for UO_2 [5]. The features observed in our PDOS calculations are in agreement with the same features calculated by Boettger and Ray [40] for bulk UO_2 and ThO_2 using

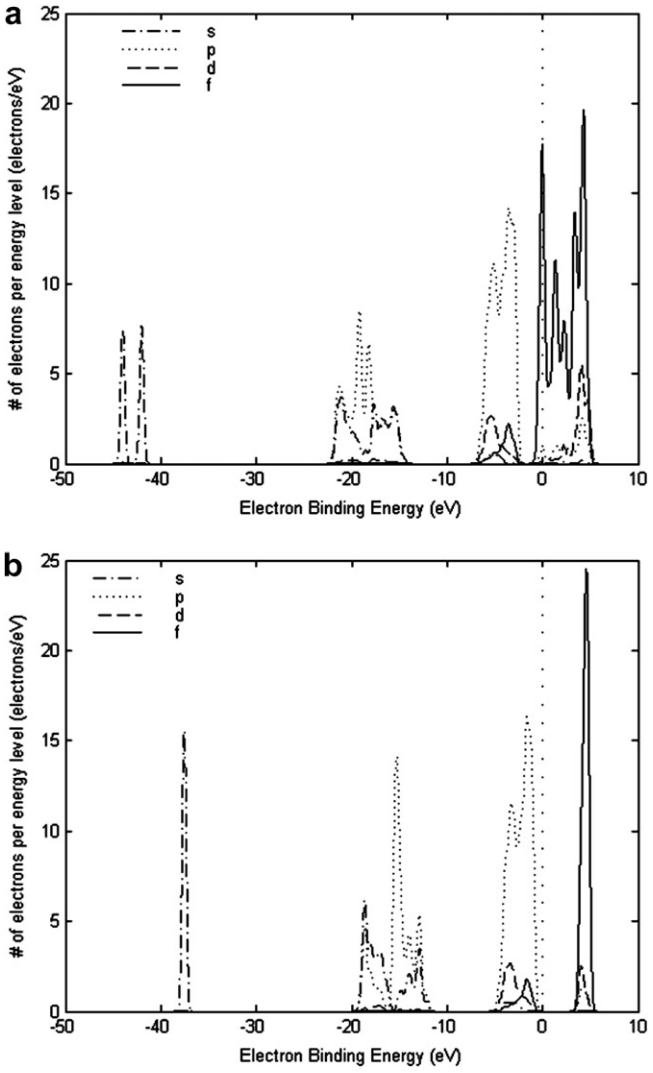

Fig. 2. Partial density of states plots (PDOS) for conventional unit cells of (a) bulk UO_2 and (b) bulk ThO_2. The dashed vertical line represents the Fermi energy (E_F) which is set to 0 eV for ThO_2, and above the U 5f orbital energy for UO_2.

quantum-mechanical methods. This agreement extends to the 5f, 6d, and 7p character of the unoccupied conduction band orbitals in our calculations. In the following sections, figures will be used to illustrate the major bonding interactions between surface atoms and adsorbates.

One limitation of our calculations is that planewave methods, without functionals to correct for the localization of f-orbitals near the metal cores, tend to underestimate the band gap of UO_2. The experimental band gap of 2.14 eV [4] in UO_2 arises due to repulsive interactions between the two unpaired uranium 5f electrons [40,56–58]. Here, UO_2 is predicted to be metallic, rather than weakly semi-conducting, with no appreciable separation between occupied and unoccupied orbitals (Fig. 2(a)). These results do not affect the interaction of the U 5f valence electrons with adsorbates, however, as the spin density for each U atom is captured correctly. Results in Fig. 2(b) correctly predict that ThO_2 is an insulator, although the band gap of approximately 4 eV is lower than the experimentally determined band gap of 6 eV [5]. As with U, spin density results for Th^{4+} demonstrate that the electronic properties of Th are represented correctly and that these calculation methods can capture the interaction between UO_2 and ThO_2 surfaces with adsorbates.

3.2. Surface energy trends and electronic structure of adsorbate-free (1 1 1) surfaces

Due to the isostructural nature of UO_2 and ThO_2, surface energy trends are expected to be similar. For comparison with quantum-mechanical calculations of UO_2 surface energies [35], a series of ThO_2 surface energy calculations were performed on the (1 1 1), (1 1 0), and (1 0 0) surfaces as a function of increasing slab thickness (Table 2). For both UO_2 and ThO_2, the (1 1 1) surface has the lowest surface energies relative to the (1 1 0) and (1 0 0) surfaces, and is interpreted to be the most stable termination (under vacuum conditions). These results are consistent with calculated and predicted trends for UO_2 surfaces [34–38,52,53]. Surface energies for UO_2 are consistently lower than for ThO_2, and as slab thickness increases, ThO_2 surface energies tend to level-off while UO_2 surface energies decrease. This pattern is attributed to the ability of the semi-conducting properties of UO_2 to lessen the effect of dangling bonds at the surface by a redistribution of the electron density which lowers surface energy [59]. One important distinction about these surface energy calculations is that they are performed under 'vacuum' conditions, rather than in the presence of adsorbates. Hydroxylation of surfaces can stabilize more reactive surfaces and influence crystal morphology [37,38], however, these topics are beyond the immediate scope of this paper.

Table 2
ThO_2 and UO_2 surface energy data as a function of slab thickness

Slab thickness (stoichiometric units)	(1 1 1) J/m^2	(1 1 0) J/m^2	(1 0 0) J/m^2
$ThO_2 \times 2$	0.81	0.98	1.55
$ThO_2 \times 3$	0.71	1.35	1.72
$ThO_2 \times 4$	0.68	1.27	1.71
$ThO_2 \times 5$	0.72	1.30	1.75
Error (J/m^2)	±0.11	±0.10	±0.17
$UO_2 \times 2$	0.59	n.a.	1.21
$UO_2 \times 3$	0.51	1.01	1.21
$UO_2 \times 4$	0.46	0.85	1.19
$UO_2 \times 5$	0.33	0.83	1.07
Error (J/m^2)	±0.13	±0.13	±0.15

Note: UO_2 data calculated in [35].

One reason that the (1 1 1) surface was chosen for this study is because of its bulk-like behavior, both in terms of relaxation and electronic structure. For UO_2, the (1 1 1) surface experiences limited atomic movement of O atoms and near-surface cations (less than 0.002 nm towards the center of the slab [35]). These measurements are in agreement with data from scanning tunneling microscopy experiments indicating that the (1 1 1) surface undergoes limited relaxation and no reconstruction upon cleaving [60,61]. In the case of ThO_2, atomic movement is slightly greater on the (1 1 1) surface than for UO_2, with atoms moving approximately 0.012 nm towards the center of the slab. The (1 1 0) surface of ThO_2 experiences the least atomic relaxation (0.005 nm), and the (1 0 0) surface the greatest, on the order of 0.031 nm towards the center of the slab. For both UO_2 and ThO_2, relaxation rather than reconstruction helps to minimize the surface energy of the (1 1 1) termination.

In Fig. 3, a comparison is made between the total density of states (DOS) for bulk UO_2 and ThO_2, and their (1 1 1) surfaces. For ThO_2 (Fig. 3(a)), the band gap between bulk and surface is nearly identical, as is the occupation of the bonding orbitals below the Fermi level ($E_F = 0$ eV). For UO_2 (Fig. 3(b)), the greatest difference between the bulk and the surface DOS occurs near the top of the valence band. Just below 0 eV, the energy gap between the occupied 5f orbitals and the empty states in the conduction band is wider in the surface case than in the bulk. There is also a shift towards higher energies (relative to the bulk) for the O2p, U6d, and 7s orbitals at −2 to −7 eV. Overall, the similarity in the electronic structure between the (1 1 1) surface and bulk UO_2 and ThO_2 helps to explain the stable, bulk-like behavior of this surface termination.

3.3. Adsorption cases

3.3.1. Case 1: Molecular water adsorption

Having established the relative stability and adsorbate-free electronic structure for the (1 1 1) surfaces of UO_2 and ThO_2, we now examine four different adsorption cases. For redox-neutral cases, such as water, our calculations suggest that adsorption occurs by similar processes on the (1 1 1) surface of UO_2 and ThO_2. Adsorption energy results for UO_2 and ThO_2 are similar in magnitude,

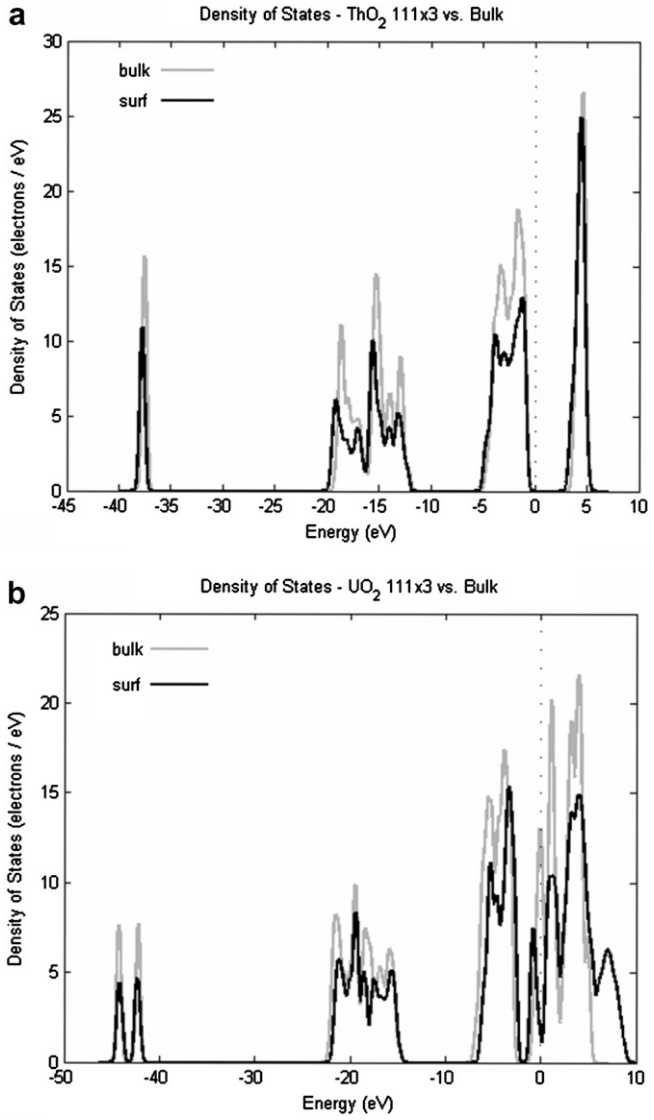

Fig. 3. Total DOS plots comparing the electronic structure of (1 1 1) surface slabs that are three stoichiometric units thick (black) *versus* the bulk (gray) for (a) ThO_2 and (b) UO_2. The dashed vertical line represents the Fermi energy (E_F) which is set to 0 eV for ThO_2 and just above the U 5f orbital energy for UO_2. The difference in DOS intensity for bulk *versus* surfaces is due to the number of atoms in each system (12 and 9, respectively).

differing by only 0.02 eV (Table 3). All values are normalized to energy per adsorption of one water molecule. $\langle U–O_{water}\rangle$ and $\langle Th–O_{water}\rangle$ distances are also similar, falling into the range of 0.26–0.27 nm. These distances are greater than $\langle U–O\rangle$ and $\langle Th–O\rangle$ bond distances in bulk UO_2 and ThO_2 (0.2362 nm and 0.2424 nm, respectively), likely due to the repulsive interactions between surface O atoms and O_{water}. The final orientation of water adsorbing onto the (1 1 1) surfaces of UO_2 and ThO_2 can be seen in Fig. 4(a) and (b), respectively. In both cases, the water molecules rotate from their original, upright positions (Fig. 1(a)) such that the hydrogen atoms in the water are closer to surface oxygen atoms in the slab. This rotation helps minimize the dipole moment perpendicular to the slab surface (Appendix A). The O_{water} remains close to the original adsorption site above the U or Th in the substrate.

Quantum-mechanical calculations allow one to investigate the electronic interactions between adsorbates and substrate atoms, in addition to providing geometric optimization data. The bubble-like features in Fig. 4(a) and (b) represent the valence band electron density for each atom. For UO_2, the top of the valence band is dominated by U 5f electrons, while for ThO_2, the top of the valence band is occupied by O 2p electrons. No significant sharing of electron density is observed between the adsorbing water molecules and the U or Th in the slab, however, the negative (favorable) adsorption energy in both cases suggests that this attractive interaction is mainly electrostatic in nature. Attractive forces could arise due to interactions between the O in water and the actinides in the slab, as well as H-bonding between the water molecule and surface O atoms.

Analysis of Mulliken spin densities (the partitioning of electron density used to determine charge and spin density for each atom [62]) in Table 4 indicates that there is no change in spin density for U atoms nearest the adsorbing water, and hence no significant electron transfer occurs. No change in the spin density can occur for Th^{4+}, since it has zero unpaired valence electrons. Due to the polar nature of water, however, the negative end of the molecule tends to repel some electron density from the metal cation that it is closest to in the slab. This effect is evidenced by small increases in Mulliken charge values for U and Th nearest the adsorbing water molecules (see Table 4), relative to adsorbate free U and Th atoms in the slab. The similarities in adsorption energies, adsorbate distances, and the lack of electron transfer during the interaction of molecular water with UO_2 and ThO_2 surfaces indicates that the adsorption of redox-neutral species is independent of electronic structure.

3.3.2. Case 2: Dissociated water adsorption

The similarity in adsorption trends for water on UO_2 and ThO_2 surfaces is also evident in the adsorption of dissociated water. While the adsorption of dissociated water is favorable on both substrates, it is 0.28 and 0.20 eV less favorable than the adsorption of molecular water on UO_2, and ThO_2, respectfully (Table 3). Molecular water is the assumed starting phase in the dissociated water case, and these negative adsorption energy results suggest that the gain in adsorption energy for dissociated water is not outweighed by the loss of energy due to dissociation. Optimized hydroxylated slabs are shown in Figs. 5(a) and (b). Adsorbate-actinide distances are similar in both of the UO_2 and ThO_2 cases, falling into the 0.22 to 0.23 nm range, which is slightly shorter than the distance between actinide atoms and O_{water} in the previous case. The closer approach of hydroxyl molecules to the UO_2 and ThO_2 (1 1 1) surface as compared with the water molecules may be due to the adsorption of dissociated H^+ cations onto surface oxygen atoms, helping to offset the negative charge of the oxygen terminated (1 1 1) surface. Alignment of surface H^+ ions

Table 3
Adsorption energies for molecular water and dissociated water cases on UO_2 and ThO_2 (1 1 1) surfaces

Case	E_{ads} on UO_2 (eV/ads.)	U-adsorbate distance (nm)	E_{ads} on ThO_2 (eV/ads.)	Th-adsorbate distance (nm)
(i) Molecular water (1/2-ML; double-sided)	−0.69	0.263 (wa)	−0.67	0.266 (wa)
(ii) Dissociated water (1/2-ML; double-sided)	−0.43	0.218 (oh)	−0.48	0.230 (oh)
Molec. water (1/2-ML) (Hay, 2006; single-sided)	−0.52[a]	0.274 (wa)[a]	na	na
Dissoc. water (1/2-ML) (Hay, 2006; single-sided)	−0.68[a]	0.222 (oh)[a]	na	na
(i) Molecular water (full-ML; double-sided)	−0.25	0.294 (wa)	na	na
(ii) Dissociated water (full-ML; double-sided)	−0.22	0.220 (oh)	na	na
			Corrected UO_2	
(i) Molecular water (full-ML; single-sided)	−0.22	0.294 (wa)	*−0.21*[b]	na
(ii) Dissociated water (full-ML; single-sided)	−0.24	0.219 (oh)	*−0.23*[b]	na

Note: Energy values are normalized to energy per single adsorbate or combination of adsorbates on each side of the slab; 1 eV = 96.489 kJ/mol.
[a] Adsorption energy values from Hay [39] were made negative to match our convention.
[b] Correction factor for single-sided UO_2 cases comes from Appendix A), Table 1A (1oh-opt-M; 1wa-opt-M).

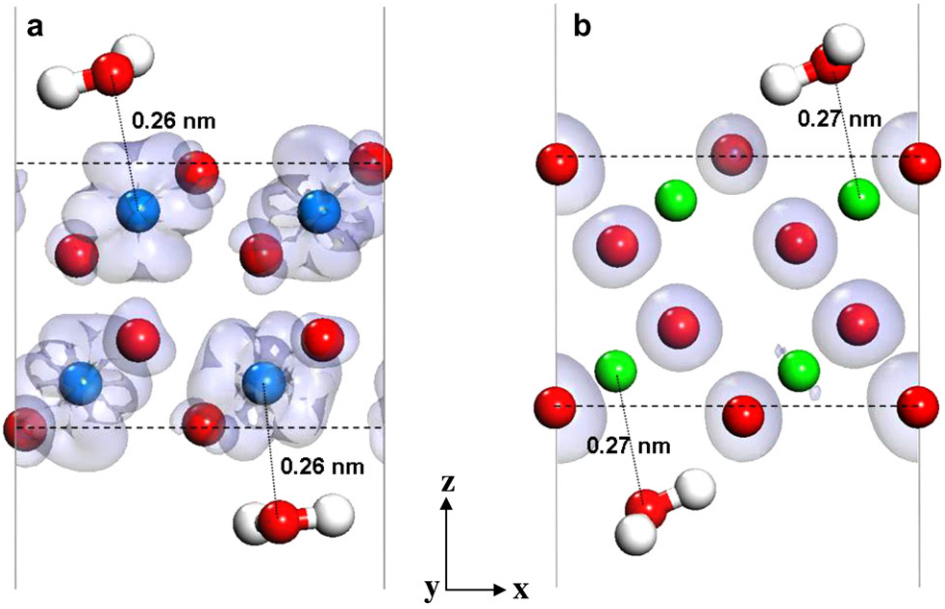

Fig. 4. Models depicting the optimized configuration of molecular water on the (1 1 1) surface of (a) UO_2 and (b) ThO_2. Dark gray spheres represent oxygen (red), outlined spheres U (blue), light gray spheres Th (green), and white spheres H. Bubble-like features represent valence band electron density which is dominated by U 5f orbitals for UO_2, and by O 2p orbitals for ThO_2, with small contributions from Th 6d and 7s. No significant sharing of electron density occurs between adsorbing water and actinide atoms in the slab. (For interpretation of the references to colour in this figure legend, the reader is referred to the web version of this article.)

in the direction of the oxygen in the adsorbing OH^- molecule suggests a possible attractive interaction between the two adsorbing species, possibly due to hydrogen bonding; ⟨O···H⟩ distances are approximately 0.16 and 0.20 nm on ThO_2 and UO_2, respectfully. ⟨O–H⟩ bond lengths for adsorbing hydroxyl molecules are slightly shorter (0.098 nm) than those for hydroxyl groups formed on the slab surface (~0.11 nm).

As in the case of molecular water, there is no significant sharing of electron valence band density between adsorbing hydroxyl molecules and actinides in the substrate (Fig. 5). Again, the top of the valence band in the UO_2 case is dominated by U5 f electrons, and by O 2p electrons for ThO_2. The negative (or favorable) adsorption energies for these cases indicate that energy-lowering interactions between slab atoms and adsorbates must be due to a combination of electrostatic forces and hydrogen bonding. There is no change in spin density for U that would indicate oxidation (see Table 4), consistent with the redox-neutral nature of hydroxyl species. As with molecular water, the adsorption of redox-neutral species appears to be independent of substrate electronic structure. However, the polar nature of hydroxyl and water molecules leads to changes in electron density surrounding U and Th atoms closest to the adsorbing species. Both U and Th atoms nearest the adsorbing hydroxyl molecules have higher charge values compared to adsorbate-free cations, indicating polarization of their surrounding electron densities (or loss of electron density;

Table 4
Mulliken charge and spin density analyses for all adsorption cases

Case	U w/o ads.	U below H_2O/OH	U below O_{ads}	O_{ads}	Th w/o ads.	Th below H_2O/OH	Th below O_{ads}	O_{ads}
(i) Molecular water	1.37/1.12	1.51/1.12	–	−0.87/−0.01	1.48/0.00	1.59/0.00	–	−0.88/0.00
	1.36/1.12	1.50/1.12	–	−0.88/−0.01	1.50/0.00	1.58/0.00	–	−0.89/0.00
(ii) Dissociated water	1.41/1.13	1.51/1.10	–	−0.84/−0.03	1.55/0.00	1.61/0.00	–	−0.92/0.00
	1.40/1.13	1.51/1.10	–	−0.82/−0.04	1.55/0.00	1.61/0.00	–	−0.92/0.00
(iii) Dissociated O_2 (high spin)	1.43/1.13	–	1.46/1.05	−0.21/0.78	1.55/0.00	–	1.49/−0.06	−0.18/0.82
	1.43/1.12	–	1.44/1.05	−0.19/0.82	1.55/0.00	–	1.49/−0.06	−0.18/0.82
(iii) Dissociated O_2 (low spin)	1.48/1.10	–	1.40/0.66	−0.33/0.24	1.57/0.01	–	1.49/−0.01	−0.25/−0.02
	1.48/1.11	–	1.40/0.65	−0.32/0.24	1.57/0.01	–	1.49/−0.01	−0.25/−0.02
(iii) Dissociated O_2 (charge transfer w/inversion center)	1.43/1.10	–	1.37/0.07	−0.28/−0.02	na	–	na	–
	1.43/1.10	–	1.37/0.07	−0.28/−0.02				
(iv) Combined H_2O and O (high spin)	–	1.53/1.12	1.40/1.06	−0.87/0.00 (wa)	–	1.60/0.00	1.51/−0.05	−0.89/0.00 (wa)
	–	1.54/1.11	1.39/1.05	−0.29/0.74 (o)	–	1.60/0.00	1.50/−0.05	−0.32/0.74 (o)
(iv) Combined H_2O and O (low spin)	–	1.57/1.07	1.38/0.69	−0.87/0.00 (wa)	–	1.63/0.00	1.53/0.00	−0.88/0.00 (wa)
	–	1.56/1.08	1.37/0.67	−0.43/0.27 (o)	–	1.61/0.00	1.55/0.00	−0.48/0.00 (o)
(iv) Combined H_2O and O (charge transfer w/inversion center)	–	1.51/0.70	1.32/0.65	−0.87/0.00 (wa)	na	–	na	–
	–	1.51/0.70	1.32/0.65	−0.41/−0.09 (o)				

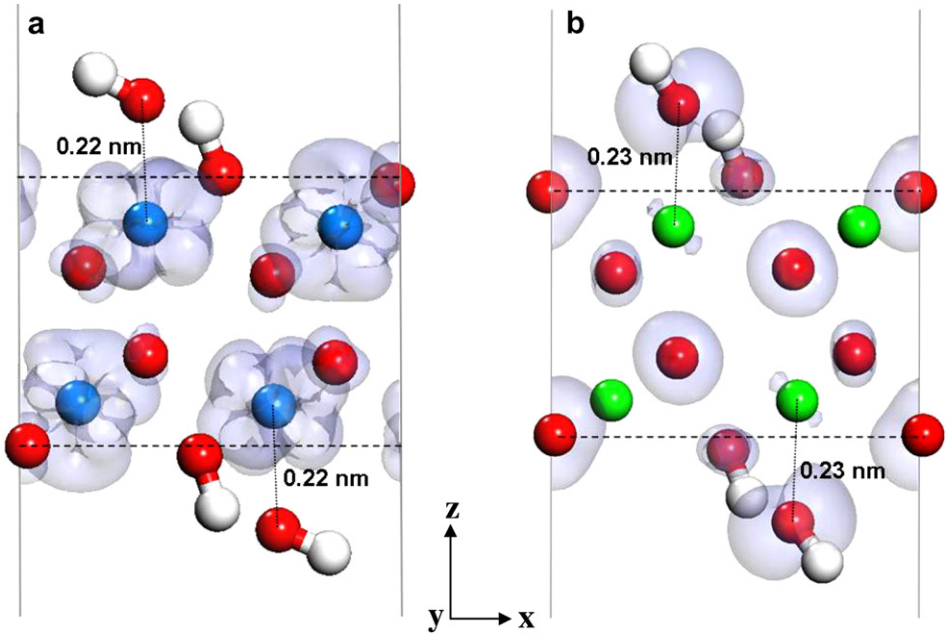

Fig. 5. Models depicting the optimized configurations of dissociated water on the (1 1 1) surface of (a) UO_2 and (b) ThO_2. Dark gray spheres represent oxygen (red), outlined spheres U (blue), light gray spheres Th (green), and white spheres H. Bubble-like features represent valence band electron density. For UO_2, U 5f orbitals dominate the top of the valence band; for ThO_2, O 2p (slab and adsorbate) and Th 6d and 7s orbitals are observed. No significant sharing of electron density is observed between the slab and adsorbates, however, some H-bonding is possible between adsorbing OH^- molecules. (For interpretation of the references to colour in this figure legend, the reader is referred to the web version of this article.)

see Table 4), due to interactions with the negative dipole end of the OH^- molecule, as is the case with the polar water molecule. While the adsorption of molecular water is slightly more energetically favorable than the adsorption of dissociated water on defect-free UO_2 and ThO_2 (1 1 1) surfaces, given the small difference in adsorption energies, a surface defect or kink site could make the adsorption of dissociated water equally or more favorable.

Comparison of our results with existing quantum-mechanical studies provides information on adsorption energy trends and magnitudes. Two previous studies have calculated adsorption energies for hydrated and hydroxylated actinide–oxide surfaces [39,40]. The similarity of our calculated adsorption energies for dissociated water on UO_2 and ThO_2 is in agreement with a quantum-mechanical study by Boettger and Ray [40], where adsorption energies for dissociated water on the (1 1 1) surface of UO_2, ThO_2 and PuO_2 were found to be nearly identical (approximately −1.16 eV (−111.9 kJ/mol) per dissociated water molecule). There too, the substrate–adsorbate interactions were deter-

mined to be independent of substrate electronic structure. In contrast, our adsorption energy trends favoring the adsorption of molecular water over dissociated water on the defect-free UO_2(1 1 1) surface are different than the adsorption energy trends calculated by Hay [39] using similar quantum-mechanical methods; a point that will be discussed in the following section.

Comparison of our results with experimental data suggests that the calculated adsorption energy values are within reason. Desorption enthalpies for reversibly adsorbed water on UO_2 and PuO_2 surfaces were measured by Paffett et al. [18] using thermal desorption mass spectroscopy. Values of 0.44 eV (42.2 kJ/mol) were reported for reversibly adsorbed water on low surface area UO_2, and similar adsorption energies of 0.69 eV (66.8 kJ/mol) and 0.43 eV (41.1 kJ/mol) were calculated in this study for molecular and dissociated water on UO_2 (1 1 1), respectively. While many experimental studies exist that explore the interaction between UO_2 surfaces and water, only a few are performed as a function of crystallographic orientation [16,19,20]. Our results are in agreement with experimental data from Senanayake and Idriss [20] for which thermal programmed desorption (TPD) results indicate that water interacts non-dissociatively with annealed, stoichiometric UO_2 (1 1 1) surfaces. In contrast, water is observed to dissociate more readily on Ar^+-sputtered UO_2 (1 1 1) surfaces which contain oxygen defects, based on observations from both X-ray photoelectron spectroscopy (XPS) and TPD. Similar results are observed by Stultz et al. [19] where TPD results indicate no significant dissociation of water on annealed UO_2 (1 0 0) surfaces, but significant amounts of H^+ generation on an Ar^+-sputtered surface with increased oxygen defects. The same trend in surface reactivity is seen regarding the interaction between carbon monoxide and stoichiometric *versus* substoichiometric UO_2 (1 1 1) surfaces [63]. For ThO_2, there are no surface-specific studies available for direct comparison; however, studies involving bulk and polycrystalline materials suggest that ThO_2 surfaces have a strong tendency to become hydroxylated [6,30,31].

3.3.3. Effects of model parameters on adsorption energy trends

In the previous section, it was noted that adsorption energy trends on the UO_2 (1 1 1) surface differ between this study and the Hay study [39], despite the use of similar quantum-mechanical methods. In both studies, planewave pseudopotential methods were used for geometry optimization of models with half-ML adsorbate coverage. The main differences between these studies are the use of single *versus* double-sided adsorption models, slab thickness (e.g. 2 *versus* 5 stoichiometric units thick), and in the Hay study [39], the bottom three units of UO_2 were held constant to mimic the effect of the underlying bulk, while all atoms were allowed to relax in our model. Yet, optimized actinide–adsorbate distances are within 0.01 nm of one another, and adsorption energies are of the same magnitude. The apparent differences in model set-up warrant further investigation because of the potential for dipole energy contributions to affect adsorption-energy trends during the use of single-sided adsorption models in a periodic set-up (Appendix A). The energy contribution from adsorbate–adsorbate interactions must also be quantified for double-sided adsorption cases (Appendix B), especially when thin slabs are being used.

In order to determine the effect of single *versus* double-sided adsorption models on adsorption energy trends, slabs with full-ML adsorbate coverage were used. Here, UO_2 (1 1 1) slabs were two stoichiometric units thick in the *z*-direction, but were not doubled in the *x*-direction. The computational parameters used were the same as for the half-ML cases. Results from our full-ML adsorption energy calculations can be seen in Table 3. In the single-sided adsorption cases, dissociated water is favored over molecular water by 0.02 eV (Table 3). This difference falls within the range of uncertainty for our calculations and suggests that the adsorption of molecular and dissociated water becomes equally likely as adsorbate coverage increases on the UO_2 (1 1 1) surface. This result is most likely due to water having more room to rotate and adsorb more closely to a surface with half-ML coverage rather than full-ML coverage. Adsorbate coverage is also found to have an effect on adsorption energy magnitudes. Specifically, adsorption becomes less favorable with increasing adsorbate coverage, likely due to increased competition for surface sites, which is consistent with catalytic studies for the adsorption of O_2 on rhodium surfaces [64].

For comparison, adsorption energy values calculated by Hay [39] for single-sided, half-ML coverage are included in Table 3, For their half-ML, single-sided adsorption cases, dissociated water is favored by approximately 0.16 eV over molecular water. This difference is similar to that which we calculated for our half-ML, double-sided adsorption cases where molecular water is favored over dissociated water by 0.26 eV. These results suggest that the use of single-versus double-sided adsorption models, as well as adsorbate coverage, can have a significant effect on adsorption energy trends, and may account for the difference in adsorption energy trends between our study and the Hay study [39]. Dipole energy contributions are discussed and quantified in the following section.

3.3.4. Adsorption energy corrections

In real crystalline materials, the adsorption of charged or polar surface species will often generate a dipole moment, which is typically neutralized by the water interface or dissolved background electrolytes. In model systems without a thick water layer and a relatively small vacuum gap to the next periodic layer, such a dipole moment can lead to an artificial (energy-lowering) slab–slab interaction energy that favors adsorbates that produce a large dipole moment. A dipole-energy correction based on dipole strength perpendicular to the slab surface, as well as vacuum gap distance, was calculated in Appendix A for

both double and single-sided adsorption models. When using double-sided adsorption models, dipole energy contributions to $E_{adsorbate+slab}$ (Eq. (1)) are ≈0.001 eV and, thus, negligible. Single-sided adsorption models can have dipole-energy contributions from slab–slab interactions of ≈0.01 eV when optimized Mulliken charges are considered. Although this energy contribution does not change adsorption energy trends for our single-sided cases, the slab interaction energy does scale linearly with dipole strength at a given separation between slabs and should be considered when using single-sided adsorption models with large dipole moments.

One of the limitations of quantum-mechanical calculations, and of the double-sided adsorption models, is that slabs cannot be made infinitely thick to represent a free surface and an underlying bulk. In cases where slabs are composed of only a few stoichiometric layers and double-sided adsorption models are used, one must always consider the possibility of energy contributions due to 'through-slab' adsorbate interactions occurring between species on the top and the bottom of the same slab. In Appendix B, the energy contribution due to 'through-slab' adsorbate–adsorbate interactions is approximated for each case. This interaction can be avoided by using single-sided adsorption models, however, one must consider the contribution due to dipole energy *versus* through-slab adsorbate–adsorbate interactions. Based on our calculations, we find that through-slab interactions are on the order of 0.002 eV or less and do not lead to changes in adsorption energy trends.

3.3.5. Case 3: Oxygen adsorption

Exploring the interaction of oxygen with UO_2 and ThO_2 surfaces using quantum mechanics provides a basis for understanding surface oxidation processes in a step-by-step manner. Thus, starting from oxygen being completely separated from the oxide surfaces as O_2, to its adsorbed state as O, we have to evaluate different spin configurations for each intermediate state to obtain the correct reaction path. At infinite distances, we consider the stability of O_2 (high-spin; ↑↑) and O_2 (low-spin; ↑↓). The high-spin (paramagnetic) state is 0.41 eV more energetically favorable than the low-spin case, as expected. Upon interacting with a UO_2 or ThO_2 surface, sequential or simultaneous O_2 dissociation and U-oxidation must occur in order for oxidation to progress, therefore different atomic oxygen cases are considered. These different atomic spin configurations are: (1) adsorption of high-spin, elemental oxygen on high-spin U in $UO_2(O^0_{hi}\uparrow\uparrow - U^{4+}_{hi}\uparrow\uparrow)$, where both O and U have a spin of two, (2) adsorption of low-spin, elemental oxygen on high-spin U in $UO_2(O^0_{lo}\uparrow\downarrow - U^{4+}_{hi}\uparrow\uparrow)$ where O has a spin of zero and U has a spin of two, and (3) adsorption of reduced, low-spin oxygen on an oxidized U site (O^{2-}_{lo} and U^{6+}_{lo}), where both O_{ads} and U_{slab} have a spin of 0. It should be noted that we only set the initial spin state of each atom; spin and charge distributions are then allowed to optimize during each run. Since Th is always in the low-spin state, we only have to distinguish a high and low spin case for atomic O on ThO_2. Adsorption energy results for each spin configuration are reported in Table 5, along with optimized actinide–adsorbate distances.

In order for the oxidation of U to occur, molecular oxygen must approach the surface and dissociate. To understand this process, two sets of calculations were performed: (1) adsorption of high-spin O_2 on the UO_2 surface as a function of distance and orientation (double-sided, full-ML), and (2) the change in energy and spin configuration for O_2 (in a box) as a function of increasing bond-length. An oxidation model describing the results is presented in Fig. 6. From our full-ML calculations, we find that O_2 is more likely to interact with the slab in a vertical geometry rather than a horizontal geometry, as depicted in Fig. 6. While adsorption energies are positive (or unfavorable) for O_2 on the UO_2(1 1 1) surface, we note changes in the spin density of the oxygen closest to the slab surface at distances less than 0.25 nm. Originally, each O atom in O_2 is assigned a spin of one (leading to an overall spin of 2; Fig. 6(a)). As O_2 gets closer to the slab (<0.25 nm), the O atom closest to the slab starts to assume a low-spin configuration (closer to a spin of 0), while the oxygen farthest from the slab acquires a greater spin density of approximately 2 unpaired spins (see Fig. 6(b)). The same sort of change in spin density distribution for O atoms in O_2 is observed upon increasing the bond-length for O_2 in the absence of a substrate (e.g. O_2 in a $1 \times 1 \times 1$ nm^3 box).

Table 5
Dry and wet oxygen adsorption energies on UO_2 and ThO_2 (1 1 1) surfaces

Case	E_{ads} on UO_2/ ThO_2 (eV/ads.)	Actinide-ads. distance (nm)	Same geom., diff. spin (eV)
(iii) Dissociated O_2 (dry)			
High spin: U^{4+}–O^o_{hi}	+2.03	0.244 (o)	+1.66 (low spin)
Low spin: U^{4+}–O^o_{lo}	+0.34	0.198 (o)	−0.07 (chg. trans.)
Chg. trans: U^{6+}–O^{2-} (w/inversion center)	−1.15	0.179 (o)	n.a.
(iv) Combined case (wet)			
High spin: U^{4+}–O^o_{hi}	+1.24 (+1.34)	0.258 (wa) 0.246 (o)	+0.50 (low-spin)
Low spin: U^{4+}–O^o_{lo}	−0.47 (−0.35)	0.259 (wa) 0.205 (o)	−0.57 (chg.-trans.)
Chg. trans: U^{6+}–O^{2-} (w/inversion center)	−2.19 (−1.84)	0.264 (wa) 0.183 (o)	n.a.
(iii) Dissociated O_2 (dry)			
High spin: Th^{4+}–O^o_{hi}	+2.11	0.246 (o)	+2.60 (low-spin)
Low spin: Th^{4+}–O^o_{lo}	+2.58	0.236 (o)	n.a.
(iv) Combined case (wet)			
High spin: Th^{4+}–O^o_{hi}	+1.18 (+1.44)	0.263 (wa) 0.252 (o)	+1.32 (low-spin)
Low spin: Th^{4+}–O^o_{lo}	−0.22 (+1.91)	0.263 (wa) 0.295 (o)	n.a.

Note: Energy values are normalized to energy per single adsorbate or combination of adsorbates on each side of the slab; 1 eV = 96.489 kJ/mol. For UO_2 and ThO_2 co-adsorption cases, values in parentheses are the sum of the individual molecular water and atomic oxygen adsorption energies.

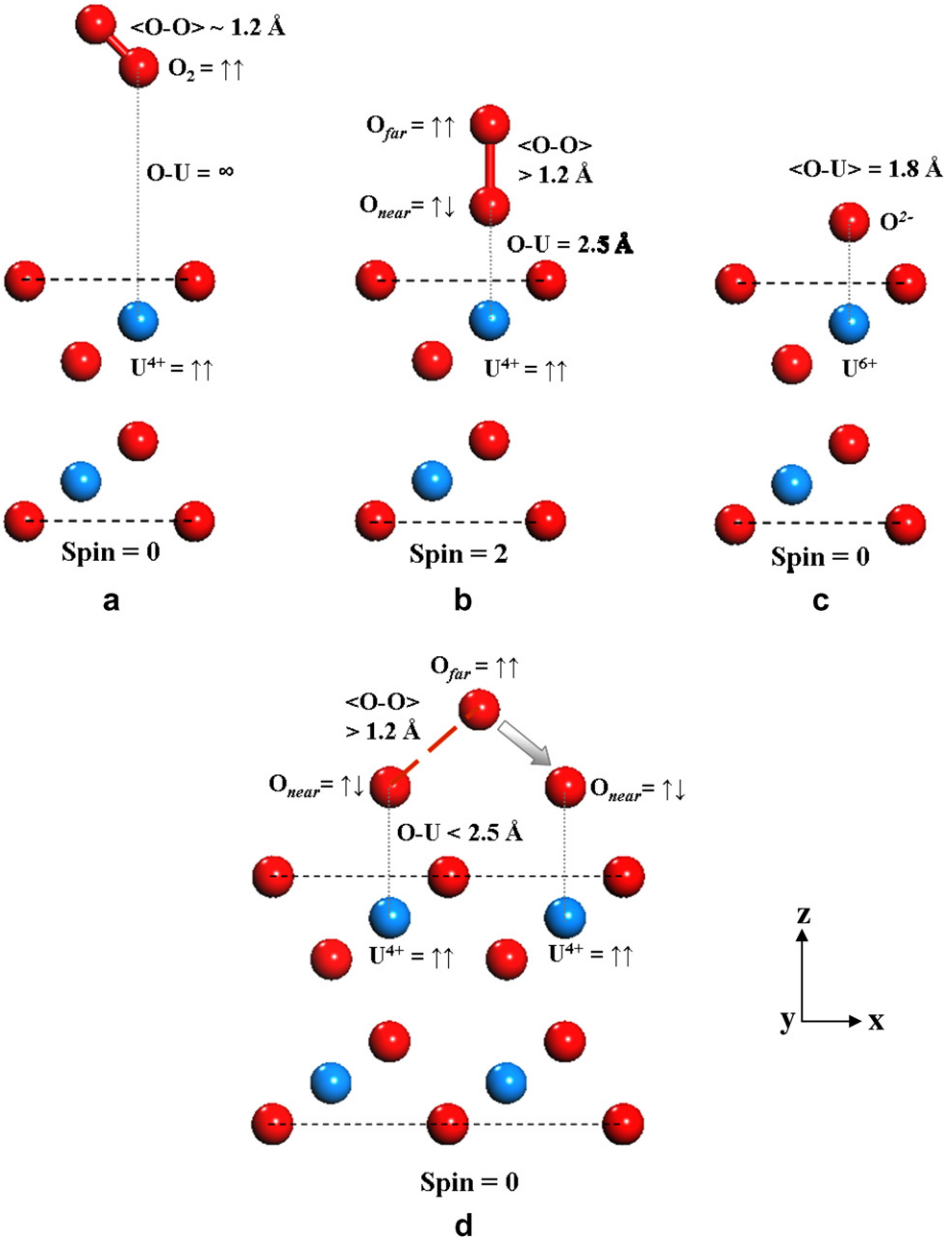

Fig. 6. Step-by-step depiction of the oxidation of the UO_2 (1 1 1) surface with full-ML coverage, starting with O_2 at an infinite distance (a). In (b), the interaction of O_2 with the UO_2 surface leads to an increase in the ⟨O–O⟩ bond-length, and a change in the spin distribution for each O in O_2. Ultimately, O_2 dissociates with $O_{low\text{-}spin}$ closest to the slab surface oxidizing U^{4+} to U^{6+}, and getting reduced to O^{2-} (c). If half-ML coverage is considered (d), $O_{high\text{-}spin}$ in O_2 may approach the UO_2 surface more closely during the dissociation process, assume a low-spin configuration, and start to oxidize U upon dissociation. Light spheres (blue) represent U; dark spheres are O (red). (For interpretation of the references to colour in this figure legend, the reader is referred to the web version of this article.)

For bond-lengths of 0.20 nm or greater, one O atom assumes a low-spin configuration and the other a high-spin configuration; as bond-length increases, the covalency of the ⟨O–O⟩ bond also decreases. The same changes in bond-length were not observed for the previously mentioned O_2 adsorption cases because they were performed under static geometry conditions.

One possible oxidation scenario is that when molecular oxygen approaches a UO_2 surface, the O atom closest to the slab will assume a low-spin configuration, and the O farthest from the slab, a high-spin configuration. As the O_2 bond length increases, dissociation will eventually occur, leading to a single low-spin O atom adsorbed onto the surface, which can start to oxidize the near-surface U (Fig. 6(c)), and one high-spin O free to recombine with other high-spin O atoms to form O_2 (high-spin). If surface sites are available (e.g. half-ML adsorption case), this high-spin oxygen may approach the UO_2 surface (e.g. during the dissociation process), assume a low-spin configuration, and start to oxidize a U atom in the slab (Fig. 6(d)). Another possibility is for U oxidation to occur simultaneously with O reduction and O_2 dissociation *via* a two-step electron

transfer process. In either case, results for U spin-density in molecular and atomic adsorption cases suggest that the presence of low-spin atomic oxygen is a necessary precursor to U oxidation.

In Fig. 7, adsorption energies are plotted with respect to a base line energy ($UO_2 + O_2$ at infinite distance – both high-spin); a threshold that must be crossed in order for oxidation to be considered energetically favorable. At a distance of approximately 0.25 nm, high-spin atomic oxygen ($O_{ads}\uparrow\uparrow$) finds a local energy minimum with respect to the UO_2 surface; however, the adsorption energy is positive, and no charge transfer occurs. At this distance, a low-spin charge configuration for $O_{ads}(\uparrow\downarrow)$ is more energetically favorable, and some charge transfer begins to occur. If allowed to relax further, $O_{ads}(\uparrow\downarrow)$ finds its energy minimum at approximately 0.20 nm. Here, charge transfer is observed between U_{slab} and O_{ads}, leading to the formation of one U^{5+} below each adsorbate, and partially reduced, O_{ads}. These results suggest that a low-spin O on a high-spin UO_2 can initiate the charge transfer process. Although this low-spin state may not be as important for the overall adsorption energy, and thus for the thermodynamics of the system as the charge-transfer case described below, it is crucial in evaluating the transition state and, thus, the kinetics of the system. Strictly speaking, the high-to-low spin transition violates the law of conservation of angular spin momentum of the system: starting from a $U\uparrow\uparrow$–$O\downarrow\downarrow(S=0)$ state to a $U\uparrow\uparrow$–$O\downarrow\uparrow(S=2)$ transition state and ending up in a final $U\downarrow\uparrow$–$O\downarrow\uparrow(S=0)$ adsorption state. However, Becker et al. [42] have shown that the lost spin momentum is easily taken up by, e.g. corner or kink sites that are present on any surface.

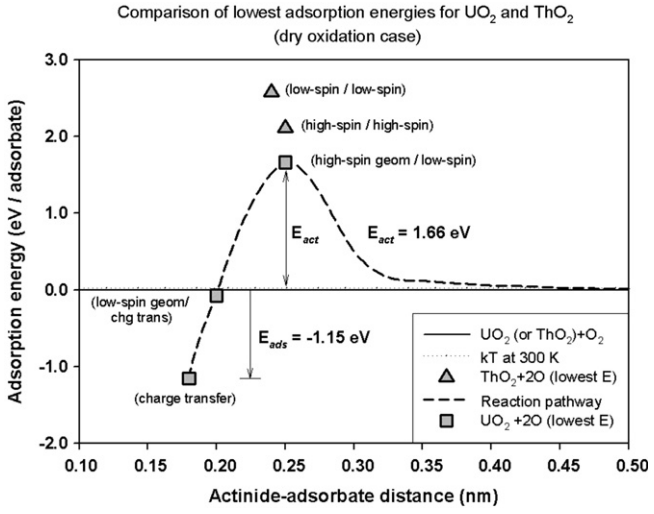

Fig. 7. Plot depicting the stability of dissociated oxygen as a function of spin configuration on the (1 1 1) surfaces of UO_2 and ThO_2. The solid horizontal line represents the energy of UO_2 or ThO_2 in the presence of O_2 (high-spin) at infinite distance. The dotted horizontal line represents kT at room temperature (~0.026 eV). The curved, dashed line represents a hypothetical reaction pathway for oxidation of the UO_2 surface once dissociation of O_2 occurs. Gray squares represent optimized U-adsorbate distances for the high-spin, low-spin, and charge-transfer starting models; the lowest-energy spin configurations are plotted for each model. Gray triangles represent adsorption energies for atomic oxygen on the ThO_2 (1 1 1) surface; original high-spin and low-spin cases are plotted. Uranium oxidation is associated with crossing the UO_2–O_2 threshold. For ThO_2, the ThO_2–O_2 threshold is never crossed, and ThO_2 is not oxidized.

Finally, the charge transfer case is found to be the most energetically favorable adsorption scenario for atomic oxygen onto the UO_2 surface (U^{6+}–O^{2-}; both spin of 0), and optimized $\langle O\text{–}U\rangle$ bond-lengths are on the order of 0.18 nm. Already at 0.20 nm, this spin configuration is found to be more energetically favorable than the $\langle U^{4+}_{high} - O^{0}_{low}\rangle$ case by approximately 0.4 eV, and a final adsorption energy of −1.15 eV (per O atom) is gained with respect to the initial proposal of high-spin O_2 being separated from UO_2 (see Fig. 7). Note, there are two oxidized states of UO_2 with similar total energies: (1) each incoming O oxidizes two U atoms to U^{5+}, and (2) each O atom oxidizes one U atom to U^{6+}. Due to the small energy difference of about 0.16 eV, we found that in some of calculations, these two states co-exist, with the U^{6+} configuration producing somewhat shorter $\langle U^{6+}\text{–}O\rangle$ bond distances of 0.179 nm, rather than 0.180 nm as in the $\langle U^{5+}\text{-}O\rangle$ case. The oxidation of U atoms directly below adsorbing oxygen is expected, but the wider-spread oxidation suggests that there may be a near-surface transfer of electron density in the presence of a strong oxidant; this point will be discussed later. In Fig. 8, the optimized geometry and electron density associated with the charge transfer case is depicted. These results provide an atomic-scale understanding of the electronic processes leading to the first steps of UO_2 oxidation.

The same atomic oxygen calculations were performed for the ThO_2–oxygen system and are plotted in Fig. 7 for comparison. As with the UO_2–oxygen system, at infinite distances (assuming no interaction between oxygen and the ThO_2 slab), the co-existence of molecular (high-spin) oxygen with the ThO_2 slab is more energetically favorable than low-spin O_2. Unlike the UO_2 system, however, the ThO_2–O_2 threshold is never crossed by dissociated oxygen on the surface of ThO_2. The interaction of high-spin and low-spin atomic oxygen with ThO_2 results in positive adsorption energies which are similar in magnitude, and $\langle Th\text{–}O_{ads}\rangle$ distances of approximately 0.25 nm. These results are in accordance with the fact that hyperstoichiometric phases of ThO_2 are not observed, due to the single oxidation state of thorium. The optimized geometry and associated electron density for the ThO_2–O_{hi} spin case is shown in Fig. 8, and no significant surface–adsorbate interaction is observed.

3.3.6. Case 4: Combined adsorption of molecular water and oxygen

In the final set of adsorption calculations, molecular water and atomic oxygen were placed on the same side of UO_2 and ThO_2 slabs, above neighboring actinide atoms, in order to simulate a corrosion scenario. The same series of initial O and U spin configurations tested in the

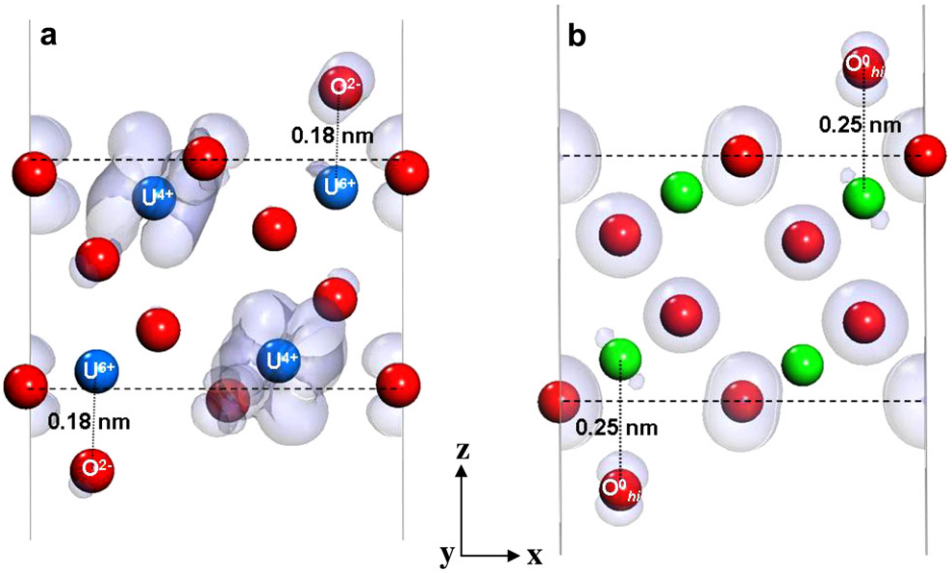

Fig. 8. Models depicting the optimized configuration of dissociated oxygen on the (1 1 1) surfaces of (a) UO_2 and (b) ThO_2. The charge transfer case is represented for UO_2 and the high-spin case is represented for ThO_2. Bubble-like features represent valence band electron density. Dark gray spheres represent oxygen (red), outlined spheres U (blue), light gray spheres Th (green), and white spheres H. In (a), the U atoms closest to O_{ads} are oxidized to U^{6+} and O_{ads} is reduced to O^{2-}; neighboring atoms retain their spin density (U^{4+}). In (b), no charge transfer occurs in the ThO_2 case and electron density in is similar to previous cases (e.g. molecular water). (For interpretation of the references to colour in this figure legend, the reader is referred to the web version of this article.)

dry-oxidation models are tested here (e.g. $O^0_{hi}\uparrow\uparrow, O^0_{lo}\uparrow\downarrow$, and O^{2-}–U^{6+}). The adsorption energies from the co-adsorption models are representative of a scenario for which oxygen and water adsorb onto the surface at the same time. These energies are compared with the sum of the individual adsorption energies for the molecular water and dry oxidation cases. Any difference in adsorption energy is interpreted either as direct adsorbate–adsorbate interactions, or in the case of semi-conducting materials such as UO_2, an additional near-surface, through-slab, adsorbate–adsorbate interaction.

Adsorption energies for the co-adsorption cases are given in Table 5. The sum of the individual molecular water and atomic oxygen adsorption energies are included below each co-adsorption energy value for comparison. Optimized geometries for adsorbates on UO_2 and ThO_2 can be seen in Fig. 9(a) and (b), respectively. For UO_2, distances between $\langle U–O_{water}\rangle$ and $\langle U–O_{ads}\rangle$ for the high-spin and low-spin co-adsorption cases are similar to those observed in the individual cases. In the low-spin oxygen case, the U atom closest to O^0_{lo} is partially oxidized to a U^{5+}-like state, and the adsorbing O atom is partially reduced, as observed in the low-spin dry oxidation case. Due to the similarity of adsorbate behavior between the individual adsorption cases and the co-adsorption cases, the lowering of energy by 0.1 eV in the co-adsorption case is attributed to direct and through-surface adsorbate–adsorbate interactions, a point that will be discussed later.

The greatest difference in adsorption energy between the co-adsorption case and the sum of the individual adsorption cases is seen in the charge-transfer calculation, where co-adsorption is favored by 0.35 eV. Mulliken charge analysis indicates that both U atoms on the UO_2 surface become oxidized to a U^{5+}-like state (Table 4). This wider-spread oxidation is in contrast to the more localized oxidation observed in the oxygen-only case, where only the U atom directly below the adsorbing O changes to U^{6+}. While a decrease in Mulliken charge-density is observed for U atoms closest to adsorbing molecular water in both the individual and co-adsorption case, this change in the near-surface electronic configuration helps to lower the activation energy for U-oxidation to occur and enhances the interaction of oxygen with the UO_2 slab surface (Fig. 9(a)). This 'surface proximity effect' [42] can occur on semi-conducting material surfaces and will be discussed in the following section. Due to the polarizing nature of dissociated water on the UO_2 surface, this effect could occur in the presence of hydroxyl groups as well.

As in the dry-oxidation case, low-spin and charge transfer spin configurations were tested for the optimized high-spin and low-spin co-adsorption geometries, respectively. The resulting adsorption energies are listed in Table 5. At distances of 0.25 nm, the activation energy barrier for U-oxidation to occur drops from 1.24 eV to 0.50 eV, if a low-spin rather than high-spin configuration is considered for the adsorbing oxygen atoms. This activation energy is 1.16 eV lower than the activation energy barrier to U-oxidation if water is not present, which is calculated to be 1.66 eV. A comparison of the lowest energy adsorption energy values is plotted for wet as compared with dry-oxidation conditions in Fig. 10. The high-spin turned low-spin energy reduction is significant

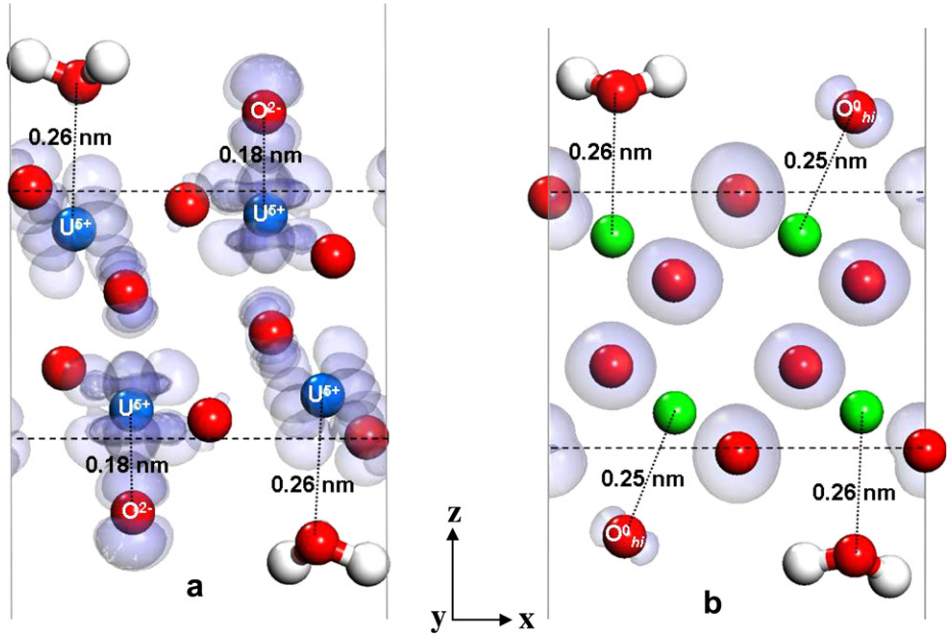

Fig. 9. Models depicting the optimized configuration and valence band electron density for (a) the charge-transfer, co-adosrption case on UO_2, and (b) the high-spin oxygen, co-adsorption case on ThO_2 (b). Dark gray spheres represent oxygen (red), outlined spheres U (blue), light gray spheres Th (green), and white spheres H. In (a), there is an increase in electron density between O_{ads} and U_{slab} relative to the dry-oxidation case, and all surface U atoms are U^{5+}. In (b), there is no significant change in near-surface electron density between O_{ads} and Th in the presence of water. (For interpretation of the references to colour in this figure legend, the reader is referred to the web version of this article.)

because this means that in the presence of water, there is a lower energy barrier to the adsorption of oxygen, thus increasing the likelihood for O_2 dissociation, O-reduction, and U-oxidation to occur on the UO_2 surface. These values can be used to calculate the probability that uranium in UO_2 will be oxidized by low-spin, atomic oxygen in the following manner.

First, we must calculate the number of O_2 molecules hitting a UO_2 surface with a given surface area (e.g. $A = 1\ nm^2$). At 25 °C, the average velocity of O_2 molecules at room temperature, according to $1/2mv^2 = 3/2kT$ is 484 m/s, where m is mass in kg, v is velocity in m/s, k is Boltzmann's constant converted to kg m/s^2 mol K, and T is temperature in Kelvin. The pressure (P) caused by N particles that hit an area, A, per second is the force, F, or the total momentum transfer per second (Nmv). Thus, $P = F/A = Nmv/A$. Assuming atmospheric pressure ($1\ atm = 10^5\ kg\ m^{-1}\ s^{-2}$) we solve for $N = (10^5\ kg\ m^{-1}\ s^{-2})(1 \times 10^{-18}\ m^2)/(0.032\ 6.022 \times 10^{-23}\ kg)\ (483\ m/s) = 3.8 \times 10^9$ O_2-molecules hitting a UO_2 surface of 1 nm^2 per second. The same calculation can be performed for atomic O and results in 5.4 times 10^9 O-atoms/(s nm^2). Here we make the assumption that every O_2 molecule hitting the UO_2 surface will dissociate. Finally, Boltzmann's equation (probability = $\exp(-E_A/kT)$ is used to calculate the probability that low-spin, atomic O will oxidize the UO_2 surface; the activation energy, E_A, comes from the adsorption energies in Table 5.

Three different cases are considered for wet and dry oxidation of the UO_2(111) surface. In the first case, we assume that atomic oxygen and molecular water co-adsorb simultaneously. Here, adsorbate–adsorbate interactions, as well as near-surface changes in electron density (e.g. due to

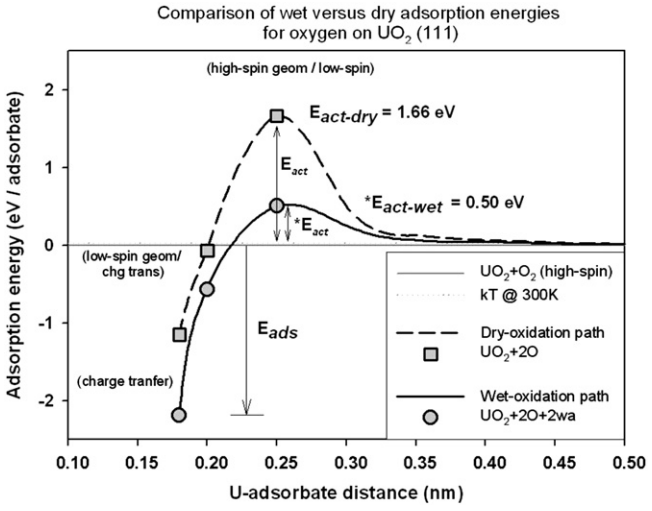

Fig. 10. Comparison of possible reaction pathways for wet-oxidation (solid) and dry-oxidation (dashed) of the UO_2 (111) surface. Circles represent adsorption energies for wet-oxidation; squares represent dry-oxidation. U-adsorbate distances were determined from optimization of high-spin, low-spin, and charge-transfer starting models; energies plotted are from the lowest energy spin configurations for each model. The solid horizontal line is the reference energy for $UO_2 + O_2$ (high-spin) at infinite separation; dotted horizontal line is kT at room temperature (300 K; ~ 0.026 eV). Note the reduction in activation energy for the wet-oxidation transition from low-spin to charge-transfer case compared to the dry-oxidation case.

the adsorption of a polar species) combine synergistically to overcome the activation energy barrier to oxidation (0.5 eV). This yields a Boltzmann probability of 4.5×10^{-9} that oxidation will occur, and when multiplied by 3.8×10^{9} O_2 molecules hitting a UO_2 surface per second, 17.1 oxidation events per second per nm^2, which is essentially spontaneous. The next wet-oxidation scenario we consider is the oxidation of UO_2 in the presence of water, but without the help from the changes in near-surface electronic structure from water or energy-lowering adsorbate–adsorbate interactions to overcome the barrier to oxidation. Specifically, the adsorption energy of water alone is added to the co-adsorption energy = 0.5 eV + 0.7 eV = 1.2 eV. Here, the probability of oxidation is 9.0×10^{-21} which yields 3.4×10^{-11} oxidation events per nm^2 per second, or, one oxidation event per nm^2 approximately every 1000 years. Finally, assuming absolutely dry conditions where the oxidation energy barrier is 1.66 eV, the likelihood of oxidation is reduced to 1.87×10^{-28}, for an oxidation rate of 7.1×10^{-19} oxidation events per nm^2 per second. Thus, oxidation of a defect-free UO_2 (1 1 1) surface under absolutely dry conditions can be ignored, and one would have to look at defects or other surfaces as potential oxidation pathways.

The same series of hi-spin and low-spin oxygen adsorption calculations were performed for ThO_2 in the presence of water. Co-adsorption energies are reported in Table 5, and the optimized geometry and the valence band electron densities for the high-spin $ThO_2 + 2O + 2wa$ case is shown in Fig. 9(b). In the high-spin adsorption case, $\langle Th–O_{ads} \rangle$ and $\langle Th–O_{wa} \rangle$ distances are within 0.006 nm of their original distances; however, the wet-oxidation adsorption energy is approximately 0.26 eV more favorable than the dry-oxidation adsorption energy. Since there is no oxidation of Th in the slab, or any significant changes in Mulliken charge densities as compared with the individual adsorption cases (Table 4), these energy differences are attributed to direct adsorbate–adsorbate interactions.

During the adsorption of low-spin oxygen onto the ThO_2 surface, a significant energy-lowering is calculated (e.g. on the order of 2 eV for the wet-oxidation adsorption energy), however, anomalously short O_{ads}–O_{slab} interactions are observed in this case while $\langle Th–O_{wa} \rangle$ distances remain the same as in the high-spin case. The Th–$O_{low\text{-}spin}$ interaction in the dry-oxidation case is taken to be more representative of the expected Th–$O_{low\text{-}spin}$ interaction in the wet-oxidation case. In summary, the energy-lowering interactions in the co-adsorption case onto ThO_2 are mainly attributed to adsorbate–adsorbate interactions, as the insulating nature of the ThO_2 slab does not facilitate near-surface changes in electronic structure as compared with calculations for the semi-conducting UO_2 slab.

These calculations provide us with rough estimates for the interaction of water and oxygen with ideal UO_2 and ThO_2 surfaces, bearing in mind that actual surfaces are not defect-free and could therefore be more reactive. For UO_2 and ThO_2, surface defects may arise from radiological sources (e.g. irradiation-induced defects) and non-radiological sources (e.g. pitting of the surface due to dissolution). Such defects could enhance surface–adsorbate interactions at the specific defect site and locally change the favorability of dissociated versus molecular water, for instance. Another factor affecting surface–adsorbate reaction rates is temperature, which over the storage-time proposed for spent nuclear fuel in a geologic repository will be in the range of 50–250 °C (~350–550 K) [65]. The calculations above represent room temperature conditions, however, dry-oxidation rates at 550 K could increase by several orders of magnitude.

Generally speaking, these results support experimental studies on the corrosion of UO_2 and spent fuel where wider-spread oxidation is observed for materials stored under wet-oxidizing, rather than dry-oxidizing environments [17,22,24,26]. Physically, these calculations demonstrate that water can enhance the oxidation of UO_2 by lowering the activation energy to O adsorption and oxidation via changes in near-surface electronic structure.

4. Implications for moisture-enhanced corrosion of UO_2

The process by which one adsorbate affects the electronic structure of the adsorption site for another adsorbate has been described as the 'surface proximity effect' by Becker et al. [42] and is a phenomenon observed on a variety of semiconducting mineral surfaces [41]. The distance-dependence of co-adsorbate interactions has been further explored by Rosso and Becker [43], and results suggest that 'surface proximity effects' are typically the strongest for next nearest neighbors, then decay in an exponential fashion. However, these interactions can be important for interaction distances up to about 2.0 nm. In UO_2 and ThO_2 slabs, $\langle U–U \rangle$ and $\langle Th–Th \rangle$ distances are 0.3866 nm and 0.3958 nm, respectively, which is within the range for surface proximity effect interactions.

While the polarizing effects of water and hydroxyls are also observed in ThO_2 slabs, the enhancement of $\langle Th–O \rangle$ interactions is not seen in the combined water and oxygen case as it is on the UO_2 case, because ThO_2 is an insulator. One reason for this difference may be that the movement of electrons in near-surface regions for UO_2 is facilitated by the weakly-semiconducting nature of UO_2, especially when surface species become oxidized and electron movement can proceed by p-type conduction (hole hopping) [5,66].

The effect of polar adsorbates on near-surface charge density observed in this study helps to explain the enhancement of UO_2 corrosion in the presence of both water and oxygen. In a study by Haschke et al. [17], a model for moisture-enhanced corrosion of uranium and plutonium metal under low p_{O_2} conditions (<15 mbar O_2) is proposed that accounts for: (1) the formation of

UO_{2+x} phases and PuO_2 accompanied by the reaction of O_2 at an accelerated rate while maintaining constant H_2O concentration, and (2) moisture-enhanced oxidation coinciding with the temperature stability range for the adsorption of water on these materials. Results from our calculations indicate that atomic oxygen and water can co-exist stably on the UO_2 surface, and the polarizing effects of water on near-surface electron density can explain why enhanced oxidation is only observed within the stability field of water. The biggest difference between the present calculations and previous models of water-enhanced corrosion of UO_2 is that the 'surface proximity effect' provides an electronic explanation for the increased interaction of oxygen with UO_2 surfaces in the presence of polar species such as water. Other multi-valent actinide oxides such as PuO_2 have been shown to demonstrate catalytic-like behavior in the presence of oxygen and water, facilitating the dissociation of water and ultimately oxidation [67]. Comparison with insulating ThO_2 surfaces indicates that the semi-conducting nature of UO_2 is crucial to this effect.

In a once-through fuel cycle, corrosion resistance is a significant factor in determining the long-term stability of spent nuclear fuel as a waste-form. Studies have demonstrated that dissolution rates decrease as Th content in UO_2 fuels increases [7–9]. Based on the resistance to corrosion exhibited by ThO_2 relative to UO_2 and the fact that the two compositions form a complete solid solution [1,2], mixed U–Th fuels may significantly improve the stability of spent nuclear fuels in a geologic repository.

5. Conclusions

Quantum-mechanical surface energies calculated for UO_2 and ThO_2 surfaces indicate that the (1 1 1) surface has the lowest energy, and is hence considered the most stable, relative to the (1 1 0) and (1 0 0) surfaces, under 'vacuum' conditions. A suite of four adsorption cases were simulated for the (1 1 1) surfaces of both UO_2 and ThO_2. When comparing the adsorption of molecular *versus* dissociated water, results suggest that on a defect-free surface, the adsorption of molecular water is more favorable on both substrates. This trend holds true for single-sided adsorption models with half-ML coverage, as well. However, as adsorbate coverage increases, the difference between adsorption energies for molecular *versus* dissociated water on the (1 1 1) surface becomes negligible, and the adsorption of either species become equally probable. The presence of defects could favor dissociated water over molecular water adsorption, even on the (1 1 1) surface. For cases where adsorbates are redox-neutral (e.g. water), adsorption energy trends are the same for UO_2 and ThO_2 and are independent of the electronic structure of the substrate.

Differences between UO_2 and ThO_2 arise when adsorbates are redox-active (e.g. dissociated O_2) and adsorption energy trends are dependent on the redox-chemistry of the substrate. UO_2 and ThO_2 also behave differently if spin transfer from or to the adsorbate is involved. When molecular oxygen (O_2) approaches UO_2 in a high-spin, paramagnetic state, the oxygen atom closest to the surface assumes a low-spin state at distances less than 0.25 nm from U in the slab. The oxygen farthest from the slab becomes more high-spin and the $\langle O–O \rangle$ bond-length increases until dissociation occurs. The presence of low-spin atomic oxygen on the UO_2 surface is accompanied by the onset of U oxidation in the slab. In the case of dry oxidation, the U atom closest to the adsorbing oxygen becomes oxidized to U^{6+} while O_{ads} is completely reduced to O^{2-}. These calculations suggest that a low-spin state of O rather than a high-spin state is a necessary precursor to adsorption and oxidation of redox-active substrates, such as UO_2. For the ThO_2-oxygen system, the ThO_2–O_2 threshold is never crossed, and therefore, ThO_2 does not become oxidized, due to the single oxidation state of thorium.

In the final adsorption scenario, the presence of water is found to lower the energy barrier for the oxidation of uranium in UO_2 and to increase the oxidation rate on a defect-free (1 1 1) surface. If atomic oxygen and water adsorb simultaneously, oxidation is essentially instantaneous (e.g. 17.1 oxidation events per second per nm^2 per year) versus the adsorption of oxygen alone where the rate on a defect-free surface is essentially negligible. The weakly semi-conducting nature of the UO_2 surface plays a role in facilitating the adsorption of oxygen in the presence of water due to near-surface changes in electron density caused by the presence of a polar adsorbate that help lower the activation energy barrier to oxygen approaching the surface and oxidizing the uranium in the slab. The 'surface proximity effect' may help explain the experimentally observed increase in oxidation rate of UO_2 in the presence of water. The same effect is not observed on the insulating ThO_2 surface. These results highlight the importance of maintaining dry storage conditions, especially under oxidizing conditions.

Finally, energy contributions from single and double-sided adsorption models were calculated in order to determine if they can have an impact on adsorption energy trends for models in a periodic setting. The energy-lowering contribution arising from the interaction between slabs is on the order of 0.001 eV for double-sided models and 0.01 eV for single-sided models. Energy contributions become more significant for systems where there is a strong dipole moment perpendicular to the slab surface. Energy contributions from the interaction of adsorbates 'through' the slab in double-sided models were found to be less than 0.005 eV, and therefore negligible. The use of double-sided models with inversion centers helps reduce the contribution of artifacts to adsorption energy calculations.

Acknowledgements

This research was performed under appointment of the Office of Civilian and Radioactive Waste Management

Fellowship Program administered by Oak Ridge Institute for Science and Education under a contract between the US Department of Energy and the Oak Ridge Associated Universities. Partial support of this research was provided from the Office of Science and Technology and International of OCRWM/DOE (DE-FC2804RW12254). FNS thanks LCS for her enthusiasm and for being a catalyst to start this project. UB is thankful for support by the National Science Foundation (EAR-0309772 and EAR-0403732). The authors thank two anonymous reviewers for their careful reading of this manuscript and thoughtful comments. The findings and conclusions of the authors of this paper do not necessarily state or reflect those of the DOE/OCRWM/OST&I.

Appendix A. Adsorption energy corrections

In an ideal system, adsorption energy would be calculated following Eq. (1). However, energy-lowering artifacts can arise due to model set-up that must be corrected for when comparing final adsorption energies. As such, we propose the following adjustments to Eq. (1):

$$E_{ads} = \frac{1}{2}\left(E_{slab+adsorbate} - E_{slab} - E_{adsorbate} - E_{int} - E_{through}\right) \quad (A.1)$$

When using vacuum gaps to simulate free surfaces in a periodic setting, an interaction energy contribution to the total energy between slabs across the vacuum gap must be considered (E_{int}). While the use of double-sided adsorption models reduces the contribution to E_{int}, the use of double-sided adsorption models also requires that a 'through-slab' energy contribution is calculated ($E_{through}$), accounting for interactions between adsorbates on the top and bottom of the same slab. The use of quantum mechanical techniques limits the number of atoms that can reasonably be included in a system; therefore, this interaction is especially important when using slabs composed of only a few stoichiometric units thick, as $E_{through}$ should decrease with increasing slab thickness.

A.1. Interaction energy between slabs

Empirical potential methods were used to calculate the interaction energy (E_{int}) between slabs in a three-dimensional periodic setting, both as a function of dipole strength and distance between slabs. Since plane-wave quantum-mechanical methods cannot be performed in a 2D setting, we used empirical potential methods to approximate the magnitude of the dipole energy contribution. To relate these results to our quantum-mechanical calculations, starting and optimized models from the full-ML, single and double-sided adsorption calculations were used (vacuum gap of 1.5 nm). Slabs with two-dimensional periodicity (e.g. where there is no vacuum gap) were generated from the slabs with three-dimensional periodicity (e.g. where slabs are separated by a vacuum gap) by 'cleaving' parallel to the top of the vacuum gap. The following equation was used to calculate the interaction energy between slabs:

$$E_{int} = E_{3D} - E_{2D} \quad (A.2)$$

In this equation, E_{int} is the difference in energy (in eV/(surface unit cell) or eV/nm^2) between slabs in a 2D periodic setting (E_{2D}) *versus* slabs in a 3D periodic setting (E_{3D}). Here, negative interaction energies represent dipole-induced attraction between slabs. Only electrostatic contributions were considered for these 'long-range' interactions across the vacuum gap ($\geqslant 1.5$ nm).

A general equation to describe the interaction energy (E_{int}) between two dipoles can be written as such:

$$E_{int} = A \cdot \mathrm{dip}^2 \cdot \left(\frac{1}{r}\right)^n \quad (A.3)$$

Here, E_{int} is reported in units of energy as a function of distance (eV/nm). The dipole moment, 'dip' is in units of 'nm unit-charge', 'r' represents the distance between two slab surfaces in nm (e.g. the vacuum gap), and 'A' is a factor in eV per surface unit charge squared, e.g. eV/(nm unit charge)^2. In a classic dipole interaction (two isolated dipoles at a distance r from each other), energy drops off as a function of ($E_{int} \propto 1/r^3$) (thus, $n = 3$). However, because our surfaces are infinite in two-dimensions and a periodic array of slabs is used, n ranges from 0.5 to 1.0 to describe the relationship of E_{int} as a function of distance. This indicates that that electric field lines are essentially parallel to one another.

Two different sets of calculations were performed, one to test the magnitude of E_{int} as a function of dipole strength squared ($E_{int} \propto \mathrm{dip}^2$), and the other to calculate E_{int} as a function of distance ($E_{int} \propto 1/r^n$). For the first case, three different charge distribution schemes were used to vary the magnitude of the dipole moment: Mulliken charges (determined from quantum-mechanical calculations) [62], formal charges, and 'charge equilibration' charges (QEq) [68] which are strongly dependent on bonding environment and electronegativity differences between neighboring atoms. Dipole moments were calculated by summing the charge contribution of each atom multiplied by its respective z-coordinate (the latter is defined to be perpendicular to the slab surface). In the second case, a charge distribution scheme was chosen, and E_{int} was calculated for each slab by incrementally increasing the vacuum gap from 1.5 to 20.0 nm.

Results from interaction energy calculations as a function of dipole strength for full-ML adsorption models are shown in Table 1A. Generally speaking, formal charge schemes lead to greater dipole moments perpendicular to the slab surfaces than QEq and Mulliken charges. Geometric optimization also serves to lower the dipole moment of each slab plus adsorbate since optimized models have smaller dipole moments than their starting-model counterparts. Interaction energy contributions are plotted as a function of (dipole strength)^2 in Fig. 1A, and the relationship is found to be linear. Dipole moments for single-sided

Table 1A
Dipole energy as a function of dipole strength (vacuum gap = 1.5 nm)

Case	Dipole (nm u.c.)	Dipole^2 (nm u.c.)^2	Dipole E (eV)
1oh-start-F	0.025	0.001	−0.036
1oh-start-M	−0.051	0.003	−0.096
1oh-start-Q	−0.033	0.001	−0.041
1wa-start-F	0.117	0.014	−0.501
1wa-start-M	0.051	0.003	−0.095
1wa-start-Q	−0.040	0.002	−0.059
1oh-opt-F	0.061	0.004	−0.130
1oh-opt-M	**0.013**	**0.000**	**−0.010**
1oh-opt-Q	−0.027	0.001	−0.028
1wa-opt-F	0.041	0.002	−0.069
1wa-opt-M	**0.0165**	**0.027**	**−0.011**
1wa-opt-Q	−0.055	0.003	−0.106
2oh-opt-M	**0.001**	**0.000**	**−0.002**
2wa-opt-M	**0.000**	**0.000**	**−0.001**

Note: F = formal charges, M = Mulliken charges, Q = charge equilibration charges; u.c. = unit charge (unitless); highlighted values apply directly to models used in this study.

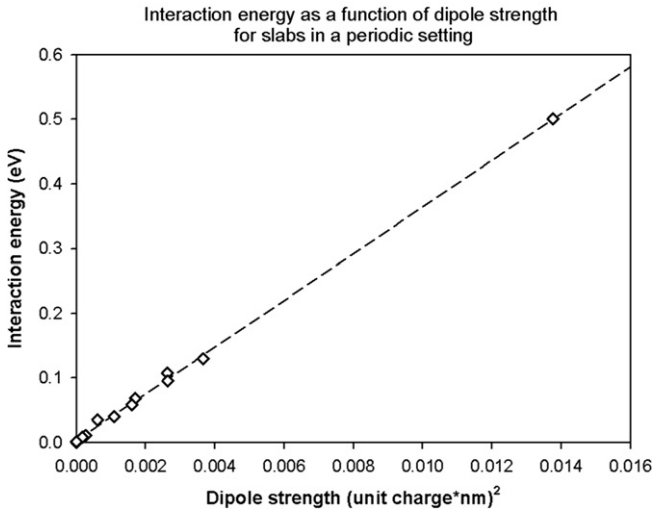

Fig. 1A. Plot illustrating the interaction energy between two slabs in a periodic setting as a function of dipole strength, derived from empirical potential calculations. Vacuum gap distance is 1.5 nm, which is applicable to quantum-mechanical calculations in the main text. Interaction energy is positively correlated to dipole moment magnitude.

adsorption cases (regardless of charge scheme) are one to two orders of magnitude greater than dipole moments for double-sided adsorption models.

In order to apply these results to our quantum-mechanical calculations, E_{int} was calculated directly for each optimized full-ML, single and double-sided adsorption model. Optimized Mulliken charge distributions for each model were used to calculate the dipole moment perpendicular to the slab surface. For double-sided adsorption models, dipole moments are on the order of 0.001, and we can show that E_{int} is of the same magnitude (e.g. 0.001 eV) and therefore makes no significant contribution to adsorption energies (see Table 1A). If symmetry is imposed during geometry optimization of these models, dipole moments should be zero. In contrast, single-sided adsorption cases tend to have larger dipole moments perpendicular to the slab surface, and this correlates to larger dipole energies. In the single-sided adsorption case for molecular water, E_{int} is on the order of 0.01 eV when using optimized Mulliken charges.

When applied to our original adsorption energy calculations (Table 3), E_{int} does not change adsorption energy trends between molecular and dissociated water in the double-sided adsorption cases, or in the single-sided adsorption cases. However, these results indicate that interaction energy contributions that arise due to a strong dipole moment perpendicular to the slab surface should be considered when using single-sided adsorption models in an infinitely periodic set-up.

Appendix B. Through-slab adsorbate interactions ($E_{through}$)

When using quantum-mechanical techniques, thin slabs are necessary in order to limit the number of atoms in the system. When combining thin slabs with double-sided adsorption models, however, an additional correction needs to be considered to account for the interaction between adsorbates on the top and bottom of the same slab. Empirical potential methods were used to approximate this 'through-slab' adsorbate–adsorbate interaction ($E_{through}$). Here, only 2D periodic models were used to avoid any interaction energy contributions from neighboring slabs across the vacuum gap. The following equation is used for this calculation:

$$E_{through} = E_{double} - 2 * E_{single} + E_{slab} \quad (A.4)$$

In order to isolate the effect of adsorbates on each other, the energy of an optimized, double-sided adsorption model is calculated (E_{double}). Then, adsorbates are removed from one side of the slab and the single-sided slab energy is calculated (E_{single}). Finally, the energy of the slab alone (E_{slab}) is calculated and added back into the equation. These calculations are again only based on electrostatic interactions, although some quantum-mechanical information is applied through the use of optimized Mulliken charges. Calculations of $E_{through}$ were performed on optimized full and half-ML cases using Mulliken charges. Prior to these calculations, charge neutrality of the system was ensured by summing the charges of both the adsorbates and the slab atoms to zero, independently. This correction was applied to all models except for the cases involving the adsorption of only oxygen since charge neutrality cannot be maintained in the single-sided adsorption portion of those cases.

In Table 2A, through-slab adsorbate interactions are shown for different adsorption cases on UO_2 and ThO_2. Interaction energies are divided by the static dielectric constant for UO_2 and ThO_2, resulting in final energies on the order of 0.002 eV. These results are two to three orders of magnitude smaller than calculated adsorption energies and are therefore considered negligible. Even when thin slabs are used, through-slab adsorbate–adsorbate interactions do not generate a significant energy

Table 2A
Through-slab adsorbate–adsorbate interactions

Case	E_{slab} (dbl. sided) (eV)	E_{slab} (single) (eV)	E_{slab} (no ads.) (eV)	$E_{through}$ (eV)	Dielectric correction (eV)
UO_2 + molecular water (full-ML)	−30.169	−29.909	−29.701	−0.052	−0.002
UO_2 + dissociated water (full-ML)	−33.715	−33.849	−33.983	0.000	0.000
UO_2 + molecular water (1/2-ML)	−60.712	−60.012	−59.263	0.049	0.002
UO_2 + dissociated water (1/2-ML)	−62.051	−62.220	−62.389	0.000	0.000
UO_2 + 2 oxygen, 2 water (high)	−62.359	−61.491	−60.624	−0.001	0.000
UO_2 + 2 oxygen, 2 water (chg. trans.)	−46.907	−45.830	−44.754	−0.001	0.000
ThO_2 + molecular water (1/2-ML)	−70.622	−69.855	−69.068	0.020	0.001
ThO_2 + dissociated water (1/2-ML)	−67.533	−67.583	−67.633	0.000	0.000
ThO_2 + 2 oxygen, 2 water (high)	−59.504	−58.451	−57.367	0.031	0.002

Note: The static dielectric constant for UO_2 is 24; for ThO_2 it is 18.9 [69].

contribution nor do they have an effect on adsorption energy trends.

References

[1] J.S. Anderson, D.N. Edgington, L.E.J. Roberts, E. Wait, J. Chem. Soc. (1954) 3324.
[2] J.S. Herring, P.E. MacDonald, K.D. Weaver, C. Kullberg, Nuc. Eng. Des. 203 (2001) 65.
[3] R.W.G. Wyckoff, Crystal Structures 1, Interscience Publishers, New York, 1963.
[4] J.C. Killeen, J. Nucl. Mater. 88 (1980) 185.
[5] B.W. Veal, D.J. Lam, Phys. Rev. B 10 (12) (1974) 4902.
[6] R.-E. Smith (Lords), J. Nucl. Mater. 328 (2004) 215.
[7] S. Sunder, N.H. Miller, J. Nucl. Mater. 279 (2000) 118.
[8] G. Heisbourg, S. Hubert, N. Dacheux, J. Purans, J. Nucl. Mater. 335 (2004) 5.
[9] P.A. Demkowicz, J.L.J. Jerden, J.C. Cunnane, N. Shibuya, R. Baney, J. Tulenko, Nucl. Technol. 147 (2004) 157.
[10] M.M. Baker, L.N. Less, S. Orman, J. Faraday Trans. 62 (1966) 2513.
[11] M.M. Baker, L.N. Less, S. Orman, J. Faraday Trans. 62 (1966) 2525.
[12] C.A. Colmenares, Prog. Solid State Chem. 15 (1984) 257.
[13] K. Winer, C.A. Colmenares, R.L. Smith, F. Wooten, Surf. Sci. 183 (1987) 67.
[14] E. Swissa, I. Jacob, U. Atzmony, N. Shamir, M.H. Mintz, Surf. Sci. 223 (1989) 607.
[15] C. Muggelberg, M.R. Castell, G.A.D. Briggs, D.T. Goddard, Surf. Sci. 402–404 (1998) 673.
[16] M.N. Heldhili, B.V. Yakshinskiy, T.E. Madey, Surf. Sci. 445 (2000) 512.
[17] J.M. Haschke, T.H. Allen, L.A. Morales, J. Alloys Compd. 314 (2001) 78.
[18] M.T. Paffett, D. Kelly, S.A. Joyce, J. Morris, K. Veirs, J. Nucl. Mater. 322 (2003) 45.
[19] J. Stultz, M.T. Paffett, S.A. Joyce, J. Phys. Chem. B 108 (2004).
[20] S.D. Senanayake, H. Idriss, Surf. Sci. 563 (2004) 135.
[21] S.D. Senanayake, R. Rousseau, D. Colegrave, H. Idriss, J. Nucl. Mater. 342 (2005) 179.
[22] K.M. Wasywich, W.H. Hocking, D.W. Shoesmith, P. Taylor, Nucl. Technol. 104 (1993) 309.
[23] J. Nakamura, T. Otomo, T. Kikuchi, S. Kawasaki, J. Nucl. Sci. Technol. 32/4 (1995) 321.
[24] R.J. McEachern, P. Taylor, J. Nucl. Mater. 254 (1998) 87.
[25] G. Sattonnay, C. Ardois, C. Corbel, J.F. Lucchini, M.-F. Barthe, F. Garrido, D. Gosset, J. Nucl. Mater. 288 (2001) 11.
[26] A. Leenaers, L. Sannen, S. Van den Berghe, M. Verwerft, J. Nucl. Mater. 317 (2003) 226.
[27] S.D. Senanayake, G.I.N. Waterhouse, A.S.Y. Chan, T.E. Madey, D.R. Mullins, H. Idriss, Catal. Today 120 (2007) 151.
[28] J.M. Haschke, J. Nucl. Mater. 344 (2005) 8.
[29] H.F. Holmes, E.L.J. Fuller, R.B. Gammage, C.H. Secoy, J. Colloid Interf. Sci. 28 (3/4) (1968) 421.
[30] R.B. Gammage, W.S.J. Brey, B.H. Davis, J. Colloid Interf. Sci. 32 (2) (1970) 256.
[31] E.L.J. Fuller, H.F. Holmes, R.B. Gammage, J. Colloid Interf. Sci. 33 (4) (1970) 623.
[32] M. Breysse, B. Claudel, P. Meriaudeau, J. Chem. Society-Faraday Trans. I 72 (1974) 1.
[33] E.L.J. Fuller, Langmuir 19 (2003) 5052.
[34] M. Abramowski, R.W. Grimes, S. Owens, J. Nucl. Mater. 275 (1999) 12.
[35] F.N. Skomurski, R.C. Ewing, A.L. Rohl, J.D. Gale, U. Becker, Am. Mineralogist 91 (2006) 1761.
[36] A.H.H. Tan, M. Abramowski, R.W. Grimes, S. Owens, Phys. Rev. B 72 (3) (2005) 035457.
[37] M. Abramowski, S.E. Redfern, R.W. Grimes, S. Owens, Surf. Sci. 490 (2001) 415.
[38] A.H.H. Tan, R.W. Grimes, S. Owens, J. Nucl. Mater. 344 (2005) 13.
[39] J.P. Hay, in: J.L. Sarrao, S.J. Schwartz, M.R. Antonio, P.C. Burns, R.G. Haire, H. Nitsche (Eds.), Material Research Society Symposium Proceedings, 2006, p. 363.
[40] J.C. Boettger, A.K. Ray, Int. J. Quantum Chem. 90 (2002) 1470.
[41] K.M. Rosso, U. Becker, M.F.J. Hochella, Am. Mineralogist 84 (10) (1999) 1549.
[42] U. Becker, K. Rosso, M.F.J. Hochella, Geochim. Cosmochim. Acta 65 (16) (2001) 2641.
[43] K. Rosso, U. Becker, Geochim. Cosmochim. Acta 67 (5) (2003) 941.
[44] P. Hohenberg, W. Kohn, Phys. Rev. B 136 (1964) B864.
[45] W. Kohn, L.J. Sham, Phys. Rev. 140 (1965) A1133.
[46] C.J. Pickard, in: B. Winkler (Ed.), Second Kiel Workshop on the Application of Computer Simulations to Crystallography, 1998, p. 37.
[47] J.P. Perdew, Y. Wang, Phys. Rev. B 33 (1991) 8800.
[48] V. Milman, B. Winkler, J.A. White, C.J. Pickard, M.C. Payne, E.V. Akhmatskaya, R.H. Nobes, Int. J. Quantum Chem. 77 (2000) 895.
[49] M.D. Segall, P.J.D. Lindan, M.J. Probert, C.J. Pickard, P.J. Hasnip, S.J. LClark, M.C. Payne, J. Phys.: Condens. Mat. 14 (11) (2002) 2717.
[50] M.C. Payne, M.P. Teter, D.C. Allan, T.A. Arias, J.D. Joannopoulos, Rev. Mod. Phys. 64 (1992) 1045.
[51] J.R. Rustad, in: R.T. Cygan, J.D. Kubicki (Eds.), Molecular Modeling Theory: Applications in the Geosciences, vol. 42, Mineralogical Society of America, Washington, DC, 2001, p. 169.
[52] P.W. Tasker, J. Phys. C: Solid State Phys. 12 (1979) 4977.
[53] P.W. Tasker, Surf. Sci. 87 (2) (1979) 315.
[54] J. Goniakowski, M.J. Gillan, Surf. Sci. 350 (1–3) (1996) 145.
[55] L.E. Cox, W.P. Ellis, R.D. Cowan, J.W. Allen, S.-J. Oh, I. Lindau, B.B. Pate, A.J. Arko, Phys. Rev. B 35 (11) (1987) 5761.
[56] P.J. Kelly, M.S.S. Brooks, J. Chem. Society, Faraday Trans. II 83 (1987) 1189.
[57] T. Petit, B. Morel, C. Lemaignan, A. Pasturel, B. Bigot, Philos. Mag. B 73 (6) (1996) 893.

[58] S.L. Dudarev, D.N. Manh, A.P. Sutton, Philos. Mag. B 75 (5) (1997) 613.
[59] J.P. LaFemina, C.B. Duke, J. Vac. Sci. Technol. A 9 (3) (1991) 1847.
[60] M.R. Castell, C. Muggelberg, G.A.D. Briggs, D.T. Goddard, J. Vac. Sci. Technol. B 14 (2) (1996) 966.
[61] M.R. Castell, C. Muggelberg, S.L. Dudarev, A.P. Sutton, G.A.D. Briggs, D.T. Goddard, Appl. Phys. A 66 (1998) S963.
[62] R.S. Mulliken, J. Chem. Phys. 23 (1955) 1833.
[63] S.D. Senanayake, A. Soon, A. Kohlmeyer, T. Söhnel, H. Idriss, J. Vac. Sci. Technol. A 23 (4) (2005) 1078.
[64] O.R. Inderwildi, D. Lebiedz, O. Deutschmann, J. Warnatz, J. Chem. Phys. 122 (2005) 1.
[65] J. Bruno, E. Cera, in: A.M. Macfarlan, R.C. Ewing (Eds.), Uncertainty Underground: Yucca Mountain and the Nation's High-Level Nuclear Waste, The MIT Press, Cambridge, Massachusetts, 2006, p. 340.
[66] D.W. Shoesmith, J. Nucl. Mater. 282 (1) (2000) 1.
[67] J.M. Haschke, T.H. Allen, L.A. Morales, Science 287 (2000) 285.
[68] A.K. Rappe, W.A.I. Goddard, J. Phys. Chem. 95 (1991) 3358.
[69] J.D. Axe, G.D. Pettit, Phys. Rev. 151 (2) (1966) 676.